INTERNATIONAL JOURNAL OF HYDROGEN ENERGY 47 (2022) 35017–35037

Available online at www.sciencedirect.com

ScienceDirect

journal homepage: www.elsevier.com/locate/he

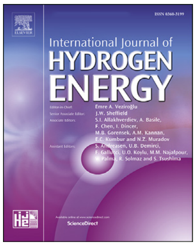

High-temperature Co-electrolysis of CO_2/H_2O and direct methanation over Co-impregnated SOEC. Bimetallic synergy between Co and Ni

Patryk Błaszczak [a,*], *Marcin Zając* [b], *Agata Ducka* [a], *Krzysztof Matlak* [b], *Barbara Wolanin* [b], *Sea-Fue Wang* [c], *Anna Mandziak* [b], *Beata Bochentyn* [a], *Piotr Jasiński* [d]

[a] *Advanced Materials Center, Faculty of Applied Physics and Mathematics, Gdańsk University of Technology, 80-233 Gdańsk, ul. Narutowicza 11/12, Poland*

[b] *National Synchrotron Radiation Centre SOLARIS, Jagiellonian University, Czerwone Maki 98, 30-392, Kraków, Poland*

[c] *Department of Materials and Mineral Resources Engineering, National Taipei University of Technology, 1, Sec. 3, Zhongxiao E. Rd., Taipei, 106, Taiwan*

[d] *Advanced Materials Center, Faculty of Electronics, Telecommunications and Informatics, Gdańsk University of Technology, 80-233 Gdańsk, ul. Narutowicza 11/12, Poland*

HIGHLIGHTS

- Novel SOEC for co-electrolysis and methanation was fabricated.
- Addition of Co into Ni-YSZ electrode ensured higher activity.
- The change of Ni valence in the electrode has crucial influence on the activity.
- Novel discovery on the Ni–Co spinel was made while TPO studies.

GRAPHICAL ABSTRACT

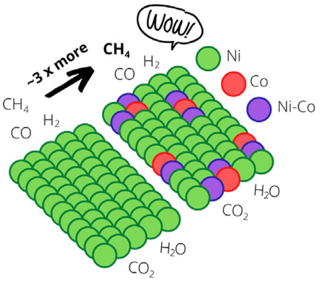

ARTICLE INFO

Article history:
Received 10 July 2022
Received in revised form
3 August 2022
Accepted 5 August 2022
Available online 31 August 2022

Keywords:
SOEC

ABSTRACT

To study the synergy between the transition metals for enhancing the electrochemical and chemical activity, a series of SOECs were modified with a small amount of Co ions, namely 1.8, 3.6, and 5.4 wt% in the reduced state. The addition of βCD into the precursor solution allowed for extremely fine dispersion of Co species across the Ni-YSZ cermet structure. The sample containing 3.6 wt% Co reached an outstanding over 2.5-times-higher concentration of CH_4 in the outlet stream. At the same time, the Co greatly enhanced the electrochemical efficiency of water and CO_2 co-electrolysis. Full characterization involving STXM imaging allowed for better understanding of the synergy between the Ni and Co host metal and made it possible to find the causes of the increased activity. It revealed the complexity of

---

* *Corresponding author.*
E-mail address: patryk.blaszczak@pg.edu.pl (P. Błaszczak).
https://doi.org/10.1016/j.ijhydene.2022.08.057

Methanation
Co-electrolysis
CH_4 yield
Catalyst
Nanoparticles

the substructures formed within the electrode. A novel discovery was described regarding the $NiCo_2O_4$ spinel structure subjected to the O_2-TPO measurements. Despite the applied oxidizing atmosphere, the catalyst evolved oxygen at elevated temperatures in a reversible manner. The performance tests indicated the roles of both rWGS and direct electrolysis of CO_2 in the electroreduction process. The addition of Co did not influence the prolonged degradation of the cell.

Introduction

Within the last few decades, rapid technological development has led to major climate changes, which are the most urgent issues that currently need to be faced. Burning carbon-derived fuels releases enormous amounts of carbon dioxide into the atmosphere, which constitutes more than 60% of global warming [1,2]. Currently, remarkable effort is being made to decrease CO_2 emissions as well as to effectively capture and store CO_2. Carbon dioxide can be used as an environmentally friendly carbon source to produce synthetic fuels and other chemicals (methane, methanol, ethanol, etc.), tackling both CO_2 capture issues and resource depletion.

Solid Oxide Electrolysis Cells (SOECs) are electrochemical devices that are able to convert water into hydrogen and oxygen by an electrolysis process occurring at the triple-phase boundary of the fuel electrode [3]. When CO_2 is fed to the electrode as an additional fuel, the co-electrolysis of CO_2/H_2O may occur. During this process, both steam and carbon dioxide undergo parallel splitting reactions resulting in the formation of a mixture of CO and H_2 (syngas) on one side and the formation of oxygen on the opposite side, which can be further utilized to produce useful chemicals [4,5]. However, due to the presence of both CO_2 and H_2 from H_2O electrolysis, the reverse Water-Gas Shift reaction (rWGS, Equation (1)) occurs simultaneously.

$$CO_2 + H_2 \leftrightarrow CO + H_2O \qquad \Delta H_{298K} = 41\ kJ\ mol^{-1} \tag{1}$$

So far, there is no agreement on the influence of rWGS on CO production: some studies show that carbon monoxide production is mainly dependent on the electrolysis, while others state that rWGS produces a significant amount of CO [6] [–] [12]. Furthermore, the total amount of CO produced depends on the temperature, voltage applied to the cell, and the composition of the inlet gases [5]. The current studies involves the modified construction of the conventional SOECs for more efficient performance when in co-electrolysis mode as well as fabrication of novel materials that will replace e.g. Ni-YSZ cermet [13–16].

The methanation reaction, in which carbon oxides are converted into CH_4, is a promising method of CO_2 utilization and also provides a solution for the transportation of low-grade energy [17]. Methanation, also known as the Sabatier reaction, can be expressed by Equation (2). For SOECs working in co-electrolysis mode, reactions of CO methanation can occur simultaneously (Equations (3) and (4)) [17] [–] [19]. As one can see from Equations (1)–(4) the methanation process is exothermic, while rWGS is endothermic, and the selectivity may be adjusted by changing the working temperature [20].

$$CO_2 + 4H_2 \rightarrow CH_4 + 2H_2O \qquad \Delta H_{298K} = -165\ kJ\ mol^{-1} \tag{2}$$

$$CO + 3H_2 \rightarrow CH_4 + H_2O \qquad \Delta H_{298K} = -206\ kJ\ mol^{-1} \tag{3}$$

$$2CO + 2H_2 \rightarrow CH_4 + CO_2 \qquad \Delta H_{298K} = -247\ kJ\ mol^{-1} \tag{4}$$

Although the methanation process is thermodynamically favorable, it is an eight-electron process, which results in the presence of a kinetic barrier [17,18,21]. To transcend this limit, the use of proper catalysts is required, among which Ni is the most commonly used, due to its high catalytic activity, selectivity, and low cost [20,22,23]. Several studies proved that the methanation is most efficient at temperatures not exceeding 400 °C, which stands in contrast with the SOEC working regime [24] [–] [27]. Moreover, at temperatures above 450 °C, the co-electrolysis reaction is favored, decreasing the selectivity of CH_4 [26,28]. In the low-temperature regime of methanation, the degradation of Ni catalysts is not significant. However, at higher temperatures of the working SOEC, Ni catalysts tend to agglomerate and coke, leading to a decrease in their performance [29] [–] [32]. J. Gao et al. showed that the addition of steam to the feed gas slightly, but not significantly, decreases the CO_2 conversion and CH_4 selectivity [24].

Other catalysts with promising properties for CO_2 electrochemical conversion, such as coking resistance, are noble metals such as Pt, Rh, and Ru [20,33]. However, their high cost considerably restricts their use for methanation [23,34,35].

Besides using monometallic catalysts, many studies are focused on incorporating a second metal, to e.g. Ni-based catalysts, to form a bimetallic system that couples the advantages of both metals. Bimetallic catalysts exhibit different catalytic properties due to modification of the electronic structure and geometry [35]. Among the most popular doping approaches, one can find the incorporation of other transition metals such as Fe or Co. Cobalt and iron can be easily dissolved in Ni metal, what can result in the formation of Ni–Co and Ni–Fe alloys and intermetallics [21]. What is more, the addition of a secondary metal may lead to increased stability and resistance to deactivation at higher temperatures [32]. Monometallic iron catalysts exhibit a high reaction rate, but low methanation selectivity, while NiFe alloys have an improved CO_2 conversion rate [21,36]. The unarguable advantage of Fe doping is its low price and high abundance. The promotion of Ni catalytic properties under the influence of Fe strongly depends on the Ni/Fe weight ratio. The work of C. Mebrahtu et al. has shown that the optimal Ni/Fe weight ratio on an (Mg, Al)O_x substrate is 0.1, while the studies by D. Pandey et al. revealed that the greatest enhancement of CH_4 selectivity and CO_2 conversion was observed for 75 wt% of Ni and 25 wt% of Fe on an alumina substrate [37,38]. The enhancement of the catalytic properties can be associated with iron ions acting as a protective element to the nickel, as suggested by M. A. Serrer et al. [39].

Another element studied as a secondary metal introduced into the Ni lattice is Co. The catalytic properties of cobalt are similar to those of nickel and its addition was shown to improve the dispersion of Ni and resistance to deactivation. Although the price of Co is higher than Ni, it is still much lower than the noble metals [22]. M. Guo et al. have shown that a small amount of Co (0.2 M Co/Ni ratio) added by impregnation to Ni/SiO_2 leads to a decrease in catalytic properties, while molar ratios higher than 0.4 enhanced the low-temperature methanation catalysis [40]. Studies by C. Jia et al. revealed that NiCo@TiO_2/SiO_2 nearly doubled the turnover frequency (TOF) compared to monometallic catalysts [41]. The enhancement in TOF values indicates that cobalt promoted the intrinsic catalytic activity as a result of a synergistic effect. Furthermore, the CH_4 selectivity was above 95% and the CO_2 conversion exceeded 50% for the aforementioned bimetallic catalysts. L. Xu et al. have synthesized NiCo on Al_2O_3 with different Co/(Ni + Co) ratios [42]. They proved that the addition of 20% Co to the total metal amount exhibits the best catalytic properties. Moreover, the synergistic effect between nickel and cobalt resulted in a decrease in the activation energy for CO_2 methanation, which further increased the CO_2 conversion rate. The addition of Co may also have a beneficial effect on the reducibility of the Ni and metal dispersion, as suggested by B. Arlafei et al. [22] However, they observed a positive influence of Co only in the case of low Ni loading (not exceeding 10% weight). It is noteworthy that long-term tests were performed on novel NiCo catalysts, proving their high stability.

So far, there has been a lack of work on the bimetallic catalysts for high-temperature methanation on Solid Oxide Electrolysis Cells. The study most similar to those presented in this article is the work of H.Y. Jeong et al., in which Fe ions were incorporated into the Ni/YSZ electrode by the wet infiltration method. They observed an increase in CO selectivity and an increase in the rWGS reaction while the SOEC was working in co-electrolysis mode [43].

Herein, a series of Solid Oxide Electrolysis Cells modified by impregnation with Co was prepared, resulting in the samples containing 1.8, 3.6, and 5.4 wt% Co metal after reduction. The changes in the phase composition and electronic structure were studied. It was found that a small amount of Co impregnated into the conventional Ni-8YSZ fuel electrode greatly enhances the performance of the SOEC for co-electrolysis of H_2O/CO_2 mixtures with direct methanation. The addition of 3.6 wt% Co resulted in a nearly 3-times higher methane peak concentration at the outlet compared to the unmodified cell. The wide variety of the characterization techniques made it possible to determine the reasons behind the enhancement being three-fold: the Co-YSZ interface increases the basicity of the cell, the formation of $NiCo_2O_4$ delivers active sites for the reactions, and the formed structures highly develop the active surface area of the electrocatalyst.

Materials and methods

SOEC modification

All electrolysers were modified by the wet impregnation method. For this purpose, a 1 M solution of $Co(NO_3)_2$ $6H_2O$ (Merck, 99.9%) in 10 v/v% EtOH in DI was prepared by dissolving the exact amount of nitrate salt in the solvent (5.82 g in 20 cm^3 of the solvent). According to our previous experience in catalyst preparation, β-cyclodextrin (βCD, Sigma Aldrich, ≥97%) was added into the precursor solution at an amount equal to 0.05 mol βCD per every mole of Co^{2+} cations (1.135 g). The native cyclodextrin acted as an ion capping agent, altering the size and dispersion of the forming nanoparticles [44].

The SOECs used in the study were delivered by the S.-F. Wang group from National Taipei University of Technology, Taiwan. The 1-inch diameter half cells were composed of a 400 μm NiO/YSZ cermet support with two different porosity levels and a 15 μm thick YSZ electrolyte. Prior to each modification step, the half cells were reduced at 850 °C under an H_2 atmosphere to further increase the porosity of the cermet layer by NiO reduction. The cells were then impregnated using 100 μL of the precursor solution, which was found to be the maximum sorption volume. The half cells were transferred to a vacuum chamber for 15 min to ensure good penetration of the precursor solution throughout the fuel electrode. The cells were dried at 120 °C and sintered under an air atmosphere at 400 °C for 4 h to decompose all nitrates and organics. A series of three samples were prepared by repeating the impregnation steps 1, 2, and 3 times, which corresponds to 1.8, 3.6, and 5.4 wt% of Co^0 in the metallic phase. A reference sample was prepared according to the same heat treatment routine but omitting the impregnation steps.

Characterization methods

X-ray diffraction patterns of the impregnated electrodes were collected using a Bruker D2 PHASER XE-T with a Cu-Kα radiation source before and after the testing procedure. The cross-sectional morphology of the pristine and spent fuel electrodes was verified using a Scanning Electron Microscope (SEM, FEI Quanta FEG 250) with an Energy-Dispersive X-ray spectroscope (EDX, EDAX Genesis APEX 2i) and Apollo X SDD detector. TEM imaging was performed using a JEOL 2100 F (Tokyo, Japan) microscope operating at 200 kV coupled with energy-dispersive X-ray spectroscopy (EDS, Oxford Instruments, UK). The X-ray Photoelectron Spectroscopy (XPS) spectra were collected using an Omnicron NanoTechnology X-ray photoelectron spectrometer with a 128-channel collector. XPS measurements were undertaken in ultra-high vacuum conditions, below 1.1×10^{-8} mbar. Photoelectrons were excited by an Mg-Kα X-ray source with the anode operating at 15 keV and 300 W. The obtained spectra were deconvoluted using the XPSPEAK41 software. X-ray Absorption Spectroscopy (XAFS) and novel Scanning Transmission X-ray Microscopy (STXM) measurements were performed at the PIRX (former PEEM/

XAS) and DEMETER beamline, respectfully, at the SOLARIS National Synchrotron Radiation Centre, Kraków, Poland [45]. The used synchrotron energy range ensured the collection of the Ni-/Co-$L_{2,3}$ and O–K edges of the as-prepared and spent cells. Powdered samples were dispersed onto carbon tape and placed on measurement plates for spectra collection. The measurements were performed using total electron yield (TEY) and/or partial fluorescence yield (PFY) using an SDD window C2 detector from Amptek depending on the self-absorption of the samples under high vacuum conditions. The energy resolution was 200 meV and better, and the beam size (h x v) was 250 μm × 40 μm. The STXM imaging was performed on powdered samples dispersed onto an Si_3N_4 membrane. The series of image stacks of the samples were collected under a He atmosphere. Detection of the transmitted radiation was performed using a photomultiplier tube. The collected images were analyzed using the aXis2000 software. Elemental maps were formed as the difference between the signals collected at the absorption peak and pre-peak energies presenting the global distribution of the selected element.

The H_2-TPR (temperature-programmed reduction) and O_2-TPO (temperature-programmed oxidation) measurements were performed using an in-house-built apparatus equipped with a TCD detector (Buck Scientific, USA), cold-trap, and a heated gas transfer line. Each time, the same amount of the sample was placed in a quartz reactor with an internal measurement of the bed temperature. The powders were degassed at 200 °C for 20 min in a stream of 5 N He prior to the measurements. The samples were reduced under a flow of 40 ml min^{-1} 5 vol%H_2 in an Ar gas mixture. The tests were performed up to 900 °C with a heating rate of 10 °C min^{-1}. Afterwards, the samples were cooled down to RT and the gas stream was switched to a mixture of 5 vol% O_2 in He. The powders were equilibrated for 1 h in an O_2–He stream and followed by oxygen uptake tests carried out using the same regime as during the TPR measurements. The profiles were collected using the PeakSimple software with a frequency of 1 Hz.

SOEC start-up procedure

Prior to each SOEC test, the LSCF ($La_{0.6}Sr_{0.4}Co_{0.2}Fe_{0.8}O_{3-\delta}$, Electro-Science Laboratories 4421A, USA) and the LSC ($La_{0.6}Sr_{0.4}CoO_3$, Fiaxell SOFC Technologies, Switzerland) layers were screen-printed onto the air-facing side of the cell with an intermediate drying step at 120 °C between each layer. The deposited pastes gave as a result of a ~30 μm thick porous base layer of LSCF underneath a ~10 μm thick LSC layer used for better electron transfer to the Au current collector. The air electrode was sintered in-situ during SOEC start-up to protect the prereduced Ni-8YSZ side from reoxidation and possible breakdown. The active surface area of the air electrode was equal to 0.78 cm^2. The SOECs were mounted onto the in-house-built measuring rig. The exact scheme of the unit and prior-measurement cell preparation steps were described in detail in our previous paper [46]. In brief, the modified SOEC was mounted onto an alumina tube and sealed using Ag-based conductive paste and dielectric ceramic adhesive (552–1105, Aremco). Au and Pt wires were used to maintain the electrical connection. The air electrode was contacted by an Au mesh and spring-loaded alumina interconnector. The set-up was placed inside a high-temperature furnace. The SOEC was each time heated up under flowing N_2 to 850 °C and then the feeding gas was switched to 47 mL_{STP} min^{-1} H_2 to perform the reduction of the modified fuel electrode material. The cell was held for 45 min at this temperature and then cooled down to 700 °C. The SOEC was equilibrated under flowing H_2 for 12 h prior to electrocatalytic tests.

Experimental procedure and test conditions

After 12 h of SOEC reduction, the gas stream was switched to a $CO_2/H_2O/H_2$ mixture. All of the gas components were dosed using electronic flowmeters. Hydrogen was supplied from the H_2 generator while the other gases were provided from pressure tanks (Air Liquide) with purity over 99.9%. The water vapor was introduced by a controlled H_2–O_2 mixture burning in an external reactor heated up to 700 °C loaded with Pt catalyst. The H_2O vapor concentration in the inlet mixture was set to 20 vol% for all runs. The rest of the inlet mixture was composed of CO_2/H_2 at a ratio of 1:2 by vol. for comparison tests. The mixture composition was chosen to be far from the equilibrium ratio (H_2:CO_2 = 4) to obtain a stronger response in CH_4 concentration change for each of the fabricated SOECs. The gas mixture was supplied at the total flow rate of 28 mL_{STP} min^{-1}. After switching to the testing mixture, the SOEC underwent conditioning at OCV until a stable voltage was achieved and later with a 1.3 V applied potential unless a stable current was observed. The resulting exhaust gases were analyzed using the FTIR-based measuring unit described in our previous work [46]. The spectrophotometer (PerkinElmer Spectrum 100) was equipped with a 10 cm length heated gas cell (60 °C) and ZnSe optical windows. The inlet/outlet flow rates were controlled using electronic flow meters. The exhaust stream was passed through a coldtrap (3 °C) followed by Nafion dryer tubing for complete water vapor removal prior to entering the FTIR. The measurements of the concentrations of gases in the outlet mixture were carried out from 700 °C down to 500 °C with a 20 °C step and 60 min delay for thermal stabilization and reaction equilibration. The spectra were collected every 5 min in the range of 4000–500 cm^{-1} with a spectral resolution of 4 cm^{-1}. Each scan was composed of five accumulations. The concentration of CO, CO_2, and CH_4 was retrieved via spectra integration performed at 3760–3520 cm^{-1} for CO_2, 2226–2143 cm^{-1} for CO, and 3250–2650 cm^{-1} for CH_4 using the SpectraGryph software and calibration curves specially designated for our set-up and presented previously elsewhere [46,47]. The amount of H_2 was determined as the difference between 100% and the sum of the CO_2, CO, and CH_4 concentrations. Simultaneously, continuous electrical measurement of the current flowing through the cell was carried out using a Gamry potentiostat/galvanostat under 1.3 V. A set of additional tests under various potentials and gas mixture ratios (maintaining 20 vol% of H_2O) was also performed. The applied potential was changed in the range of 1.1–1.6 V and the H_2/CO_2 volume ratio at 1.3 V was switched within 0.25 and 7.

The quality of the prepared cells for efficient co-electrolysis and methane production was described by means of the CO_2

conversion (X_{CO_2}), CH_4/CO yields (Y_i) and CH_4 selectivity (S_{CH_4}) catalytic coefficients calculated from the measured molar flow values using Equations (5)–(8). The yields were calculated considering the CO_2 input stream.

$$X_{CO_2}(\%) = \frac{\dot{n}^{in}_{CO_2} - \dot{n}^{out}_{CO_2}}{\dot{n}^{in}_{CO_2}} \times 100 \tag{5}$$

$$S_{CH_4}(\%) = \frac{\dot{n}^{out}_{CH_4}}{\dot{n}^{in}_{CO_2} \times \frac{X_{CO_2}}{100}} \times 100 \tag{6}$$

$$Y_{CH_4}(\%) = \frac{\dot{n}^{out}_{CH_4}}{\dot{n}^{in}_{CO_2}} \times 100 \tag{7}$$

$$Y_{CO}(\%) = \frac{\dot{n}^{out}_{CO}}{\dot{n}^{in}_{CO_2}} \times 100 \tag{8}$$

where: $\dot{n}^{out}_i$ and $\dot{n}^{in}_i$ are the molar flow rates of a specified gas (*i*) at the outlet and inlet of the reactor, respectively. The reference equilibrium compositions were calculated with the usage of the *Gem* module from the HSC Chemistry™ software. The calculations were performed under free-flow reactor conditions and atmospheric pressure for an idealized system using the Gibbs energy minimalization method disregarding the electrocatalytic reactions (OCV catalytic measurements).

Results

Phase composition and microstructure of the modified cells

The XRD patterns of the prereduced and modified SOEC fuel electrodes are presented in Fig. S1. As the NiO/YSZ composite underwent the reduction step prior to the modification steps, the phase composition consisted of ionic conductor 8YSZ (8 mol.% Yttria Stabilized Zirconia) and metallic Ni. The impregnation steps from the novel precursor solution required cyclic firing of the cermet electrode at 400 °C to decompose the cobalt nitrate and organics existing in the precursor solution. This resulted in the formation of a small amount of surficial NiO/NiOOH layer via low-temperature reoxidation of the Ni metal. Despite the introduction of the Co ions into the electrode, no additional phases were clearly distinguished from XRD measurements. It is caused by the fact that the amount of Co species present in the electrode is below the detection limit of the XRD equipment used for pattern collection. Additionally, the created species were most likely forming highly nanocrystalline objects, which in fact would produce even broader and lower in intensity diffraction peaks that could be lost within the noise. There was also no clear evidence of shifting in the peak position of the NiO/Ni lattices, even though the formation of the mixed NiO–Co_3O_4 oxide was very possible. A slight increase in the lattice parameters was observed according to the Rietveld refining method of the peaks assigned to NiO, but due to the low crystallinity of the resultant phase and broad peaks, the outcomes were designated as unreliable. Co is characterized by an infinite solubility in the Ni lattice when the metallic form is considered. The results obtained during the studies on Ni–Co alloy nanoparticles and their oxidation in the work of L. Han et al. followed by the presentation of the Ellingham and NiO_x-CoO_x phase diagram clearly indicated that within the used amounts of Co, it is highly probable to obtain mixed (Ni,Co)O monoxide with traces of metastable $NiCo_2O_4$ spinel structure [48]. Even though the XRD studies gave little information regarding the internal changes in the phase composition, they revealed the partially nanometric nature of the modified electrode due to the highly broadened peaks coming from the NiO phase.

The cross-section SEM analysis of the unmodified cell presented in Fig. S2 revealed that the microstructure of the pristine prereduced electrode consisted of micrometric grains of well-sintered 8YSZ and Ni. The NiO-YSZ composite was primarily designed to reach around 35–40% of total open porosity after the reduction. There were also two clearly distinguishable levels of porosity in the outer and functional layer (FL). The reduction step allowed for easier penetration of the infiltrant solution. The SEM images of the fractures of the reference and modified SOECs after 1, 2, and 3 impregnation procedures are presented in Fig. 1.

The structure of the electrodes differs greatly depending on the amount of introduced Co precursor solution. There are two new species clearly distinguishable in the images. The first is composed of nanoparticles of the Co oxides-hydroxides formed on the surface of the 8YSZ grains formed via non-reactive deposition. The new Co species are rather well-dispersed and clearly distinguishable on the 8YSZ grains forming uniform nanoparticles (NPs). Secondly, the paper ball-like structures that were determined to be a surficial oxide formed during the sintering steps under ambient air atmosphere. The latter one was described as Co species delivered during reactive deposition. Similar structures were also present in the reference electrode material, but of slightly less developed microstructure. Based on the simple EDX point analysis, the formed oxide scale consisted of Ni, O, and a small amount of Co. This indicated that a new structure of mixed composition formed on the surface of the Ni metal grains. The oxide scale seemed to exhibit a highly developed surface area of offbeat microstructure. The look of the scale may also stands for the formation of the spinel-like structures, as those tend to form powders of complicated morphology when in nanometric form [49,50]. Spinels are a group of materials that have been widely studied for electrochemical application by the members of our team and other international groups with groundbreaking properties followed by promising potential always being uncovered [51] [–] [53]. The arrangement of the nanoparticles on the 8YSZ grains was different for all three samples. With the increasing amount of introduced Co, the separated NPs started to form a rather continuous layer with bigger distinguishable objects. The coalescence of the repeatedly deposited Co oxides is best seen for the 5.4 wt% Co sample (Fig. 1D). In the case of reactive deposition, each additional cycle of impregnation tends to further modify the microstructure of the paper ball-like structures creating bigger, clumped-up agglomerates of Co–Ni oxides. The previously mentioned NiO_x-CoO_x phase diagram diminishes the fact of spinel formation in the homogeneous mixture. Even so, the surficial character of the Co deposition can lead to a reaction at the Ni–Co interface and form a spinel-like contact

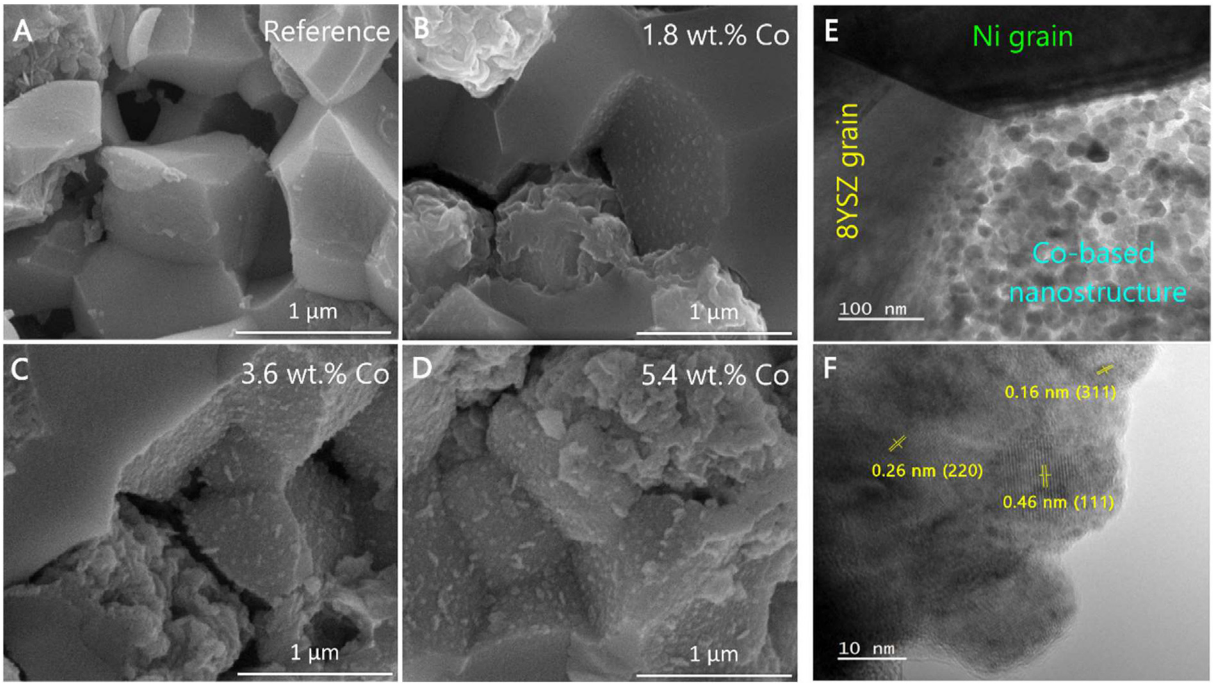

Fig. 1 – SEM images of the Co-impregnated and reference cells in 'as-prepared' state (A–D), TEM image of the 3.6 wt% Co sample at the 8YSZ-Ni-Co interface (E), and HRTEM image of the Co-based nanostructure in the corresponding sample (F).

mixed layer as those two transition metals exhibit rather high reactivity [54]. To better understand the internal structure of the modified samples, a series of TEM images (Fig. 1E and F) were captured using lamellae cut from the cells. An exemplary image of the 3.6 wt% Co sample accurately represents the general structure after Co incorporation. The imaging proved the bimodal behavior of the Co ions, i.e. reactive and non-reactive deposition. Co partially dissolves into reoxidized Ni and simultaneously forms homogeneous nanoparticles on the surface of 8YSZ. Additionally, a highly developed structure consisting of spherical polycrystalline nanoparticles was formed. The HRTEM was further utilized to analyze this porous structure deeply. From the image, we can see that the outer surface of the structure is nearly amorphous. This was caused by the low sintering temperature coupled with the addition of the cyclodextrin and most likely implies a high external active surface area [48,55]. Deeper inside, three exemplary interplanar distances were marked. The interplanar distance of well-defined lattice fringes equal to 0.46 nm was extremely close to the values observed by L. Huang et al. and A. Cetin et al., and assigned to (111) planes of $NiCo_2O_4$ [56,57]. The interplanar distances of 0.26 nm and 0.16 nm corresponded to the (220) planes of $NiCo_2O_4$ and (311) planes of Co_3O_4, respectively [58]. Slight deviation of the interplanar distances in the ideal $NiCo_2O_4$ phase arose from the nonideal stoichiometry of the compound and very probable coexistence of intermixed NiOOH–CoOOH layer double hydroxide (denoted as $NiCo_2(OH)_6$) [59]. Parallel to the mixed oxides, free Co_xO_y nanoparticles were also formed closer to the surface as the Ni ions were bound by previously deposited Co, and diffusion in the surface proximity was slowed down [60,61]. Based on those results it was stated that Ni ions are being consumed by reacting with Co ions and the surficial layer consists of finely dispersed spinel-like particles and free Co_xO_y nanoparticles. The NiO unreacted layers can be found most likely closer to the surface of the pristine Ni grains.

To quantitively study the surface composition and identify the valence state of the elements, a series of XPS measurements was performed on the as-prepared and spent electrodes (after SOEC tests). The exemplary results of the 3.6 wt% Co as-prepared sample presented in Fig. 2 shows that for both the core level spectra of Ni2p and Co2p, the peaks were fitted to the two spin-orbit doublets corresponding to $2p_{3/2}$ and $2p_{1/2}$. For each of the elements, two bands were deconvoluted after Lorentzian-Gaussian fitting and ascribed to the valence state of either +2 or +3. For Ni (Fig. 2A), the peaks located at 853.7 eV and 871.8 eV were assigned to Ni^{2+}, while the doublet around 855.4 eV and 873.2 eV to Ni^{3+}. These values are in agreement with the variety of the research dedicated to the $NiCo_2O_4$-based structures in electrocatalysis [60,62] [–] [64]. There are also two clearly visible shake-up satellite peaks within the Ni2p spectra. The slight positive shift (~0.4 eV) of the Ni^{2+} peaks in the modified samples compared to the reference also indicates the formation of a new mixed phase [60,65,66]. Moving forward to the Co2p spectra (Fig. 2B), the Co^{3+} oxidation state was indexed to the doublet located at 779.6 eV and 795.2 eV, while Co^{2+} to the one located at 781.4 eV and 797.0 eV. The position of the peaks is similar to the studies of X. Tong et al. on urchin-like $NiCo_2O_4$ and the wide range of data retrieved by other groups [60,63,67,68]. In the case of the Co2p core-level spectra, the $2p_{3/2}$ peaks are shifting towards higher binding energies of ~0.3–0.4 eV per modification step. This is also an indication of the mixed oxide phase formation and substantial decrease of Co oxidation state, i.e., taking up

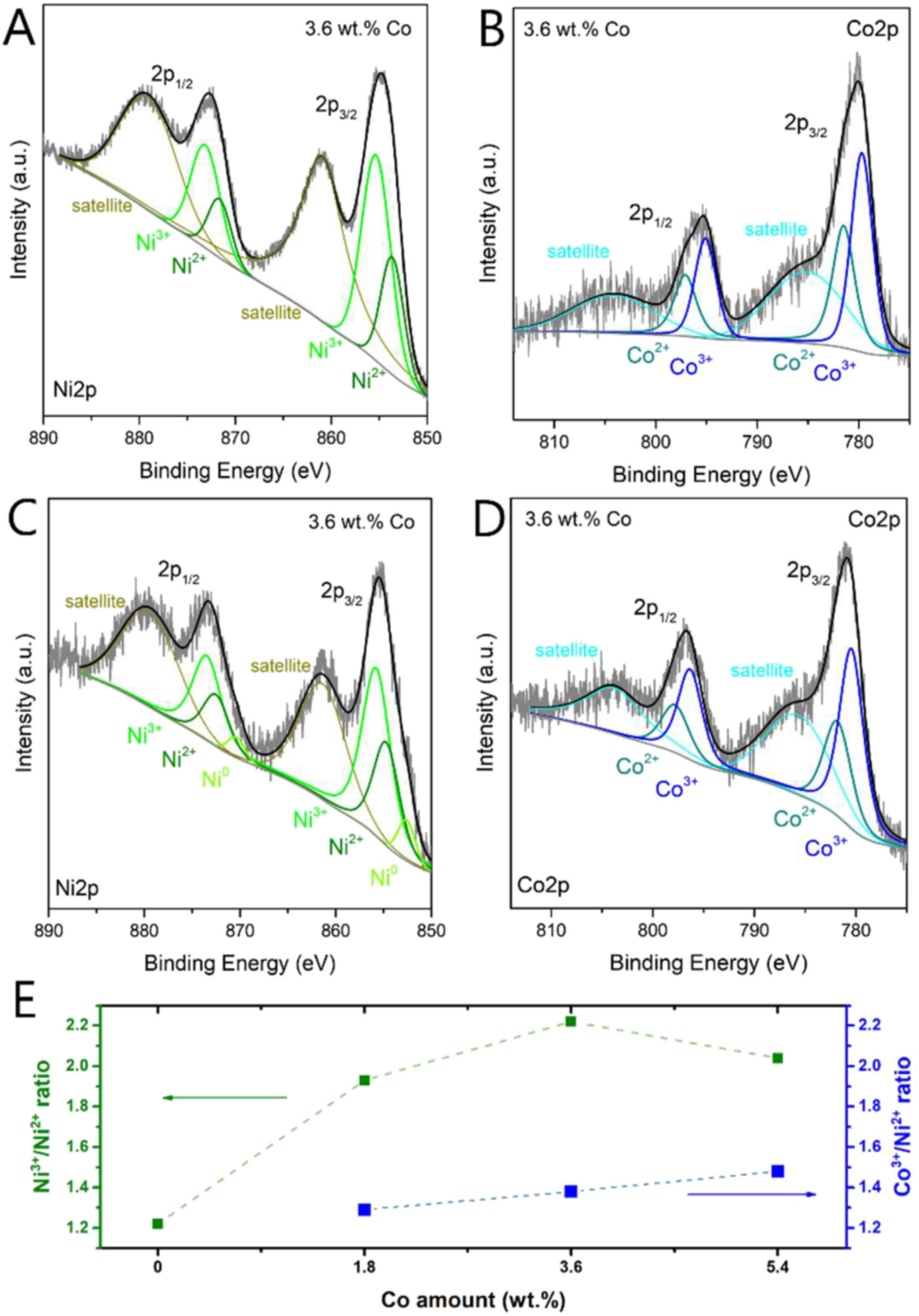

Fig. 2 – XPS spectra of 3.6 wt% Co-impregnated cell A,C) Ni2p scan, B,D) Co2p scan, and E) change of the $(Ni,Co)^{3+}/(Ni,Co)^{2+}$ ratio vs. wt.% of Co introduced. A,B – as-prepared samples, and C,D – after SOEC mode testing.

more electrons [69]. It is due to the higher amount of available Co ions and prolonged sintering time allowing for better interdiffusion. Well-fitted doublets of both elements determined the ratio of Ni^{3+} to Ni^{2+} and Co^{3+} to Co^{2+}. The changes in those ratios, depending on the amount of Co introduced, are depicted in Fig. 2E. With the increasing concentration of surficial Co ions, the ratio of Ni^{3+} to Ni^{2+} increased drastically from 1.22 up to 2.22. This directly indicates the formation of the mixed Ni–Co oxide layer, as in the case of the introduction of a minor amount of Co into NiO_x where the structure can become self-doped with Ni^{3+}. It was previously described that the Co doping of NiO results in reaching higher Ni valence states as it facilitates the formation of an Ni_2O_3 component, playing the role of p-type dopant [70] [–] [72]. A further increase of the Co amount over 3.6 wt% resulted in a slight lowering of the concentration of Ni^{3+} within the structure. A similar issue was described elsewhere and stated that the increase in the amount of free Co_xO_y clusters formed on the surface acts as a carrier trap and limits the charge transfer from Ni to Co [71]. In the case of Co, the ratio of Co^{3+}/Co^{2+} increased only slightly over the following cycles of impregnation (1.29–1.48). The same behavior was further observed and described thanks to the XAS measurements. The increase in the amount of Ni^{3+} has a substantial influence on the electrochemical performance of catalysts in oxygen evolution reaction (OER) and oxygen reduction reaction (ORR) though similar explanations may also apply in this research [73] [–] [76]. In the case of post-mortem measurements (Fig. 2C and D) it is clearly visible that an Ni metallic form came up in the XPS spectra and overpowering peaks of Ni^{3+} and Co^{3+} appeared. This is due to the presence of water vapor content in the stream during the cooling routine. It also indicates the high activity of the metals towards reacting with H_2O and the formation of NiOOH–CoOOH phases, which can have a crucial impact on the water molecules bonding during electrolysis [77].

Electrocatalytic CO_2/H_2O conversion and methane production

The electrocatalytic activity of the modified cells towards co-electrolysis with simultaneous methanation was tested under the conditions of a working SOEC. The measurements were performed under 20 vol% water vapor CO_2 stream with H_2 to prevent the oxidation of the metallic phase and ensure a higher FTIR response due to the changes in the CH_4 concentration. The testing runs were performed both under OCV and a thermoneutral bias of 1.3 V. The CH_4 concentration changes for the reference and the modified Co-impregnated cells versus SOEC temperature are presented in Fig. 3A and B. The obtained current densities shown in Fig. 3C indicated that, surprisingly, only a slight difference in the SOEC electrical efficiency was visible between the samples.

Despite their similar electrical efficiency, the CH_4 outlet concentration for the presented cells changes drastically after the incorporation of those minimal amounts of Co into the structure. The outcomes indicate superbly promising properties of the modified cells. The peaking methane concentration at OCV for the sample containing 3.6 wt% Co in the reduced state reached an outstanding 2.1% being over 2.5 times the value of the unmodified cell (~0.8%). In the case of the 1.8 and 3.6 wt% Co-impregnated cells, the maximum concentration peak shifted towards a slightly higher temperature compared

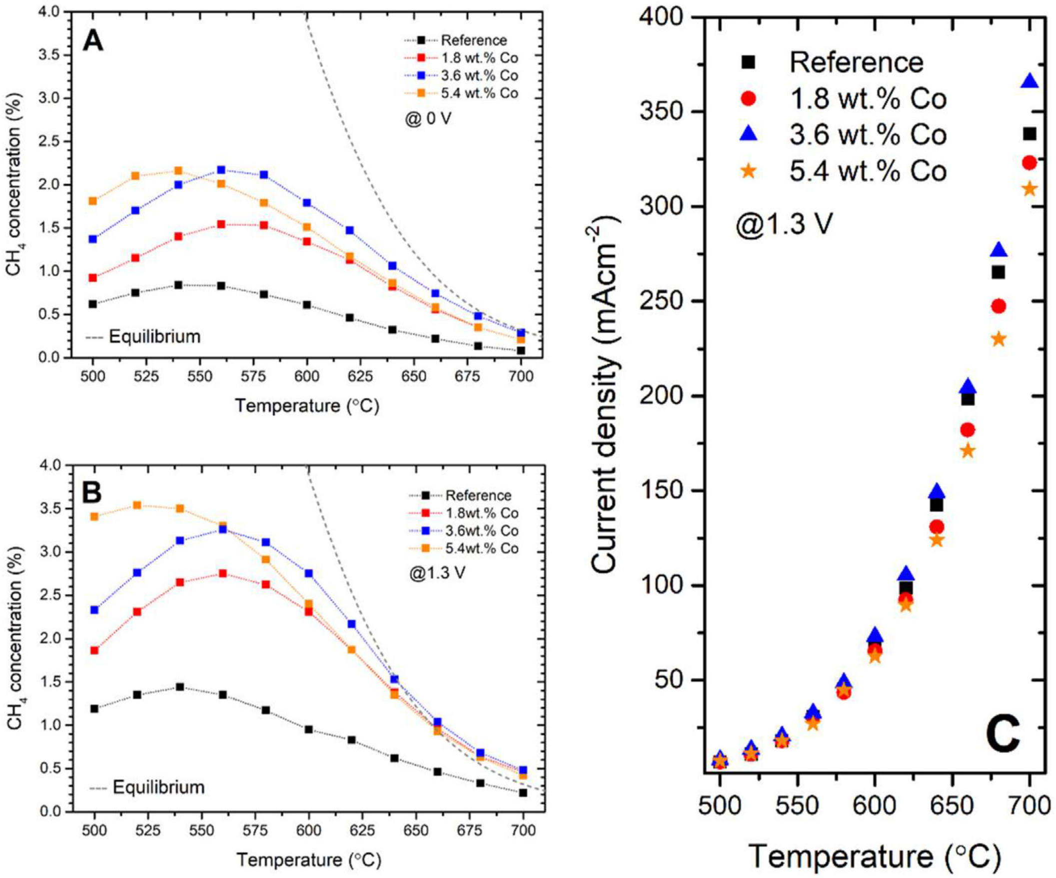

Fig. 3 – Concentration of CH_4 in the outlet stream at OCV (A) and 1.3 V (B). Equilibrium concentration marked as dashed line. (C) Current densities at 1.3 V vs. temperature. Dashed lines are visual guides only.

to the reference. It was caused by higher efficiency in the electrocatalytic CO_2/H_2O mixture splitting overcoming the existing thermodynamic limitations of the methanation reaction at high temperatures. Generally speaking, those samples exhibited elevated catalytic activity at the temperature range suitable for the proper work of an SOEC. To better represent the increase in catalytic activity, a series of describing parameters (CH_4 yield, CO_2 conversion, CH_4 selectivity, and CO yield) were calculated, and the results are depicted in Fig. 4. All of the calculations were done for the samples subjected to the tests at 1.3 V applied bias. The dashed lines were added as a visual guide to better represent the general trends. The efficiency of methane generation was determined by means of the CH_4 yield parameter. At 1.3 V and a temperature equal to around 640 °C, all of the new cells easily reached the thermodynamic equilibrium compositions simulated for the idealized systems, in contrast to the reference cell. The reason was most probably two-fold. Firstly, the modified cells in fact reached a higher level of electrochemical efficiency, which can be best seen in Fig. 4. Secondly, the methane-formation kinetics improved as the CO_2 conversion coefficient greatly increased. As the CO_2 conversion went significantly over the level of the simulated thermodynamic equilibrium, the direct CO_2 hydrogenation reaction in particular had to be facilitated by the novel composition of the working electrode. At the same time, relatively comparable currents indicated the tendency of the Co-impregnated samples to alter the ratio of electrolyzed H_2O and CO_2 towards the second component. In the case of the modified samples, there was an outstanding, over twofold increase in methane yield. The efficiency of the methanation was clearly enhanced with subtle shifts in the maximum point. The cells with 1.8, and 3.6 wt% Co revealed altered temperature-dependent catalytic response. Further addition of the Co into the structure did not increase the methane yield greatly but definitely changed the general activity look of the profile to be more like the non-modified sample. The aim of this study was to increase the high-temperature co-electrolysis and methanation efficiency (>600 °C), so the 3.6 wt% Co-impregnated sample was chosen as the most promising one. Moving on to the CH_4 selectivity, the samples were following similar trends as in the case of the CH_4 yield. There is clear and visible evidence of the increased efficiency of methane formation at elevated temperatures. Even more pronounced is the activity of the 5.4 wt% Co impregnated cell, but the shifting to the lower temperature range is also noticeable. This could be further explored regarding the methanation catalysts working under conventional conditions. For both the reference and modified samples, the evidence of electrolysis is indisputable. In all cases, the CO_2 conversion and CO yield parameters are placed high

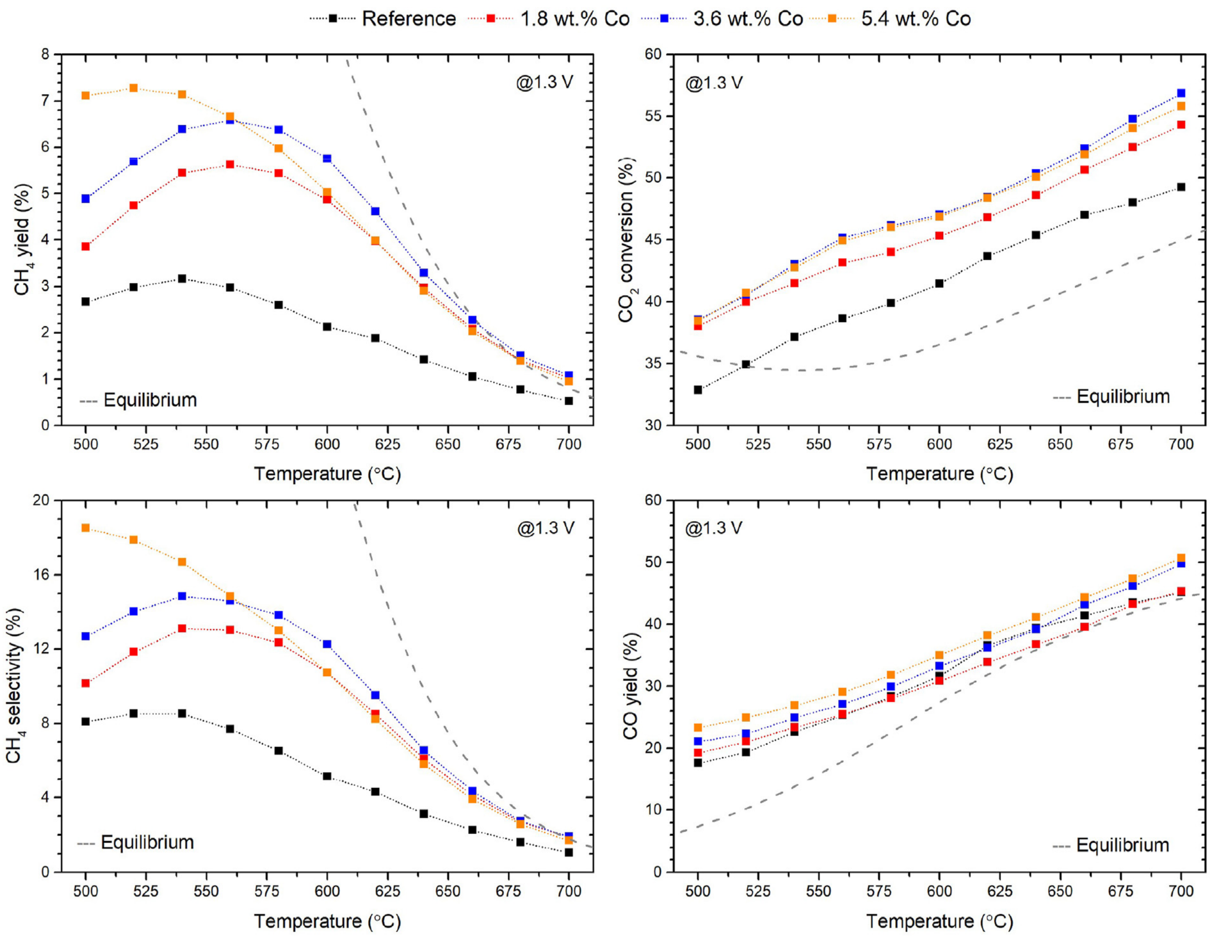

Fig. 4 – CO_2 conversion (left) and CH_4 selectivity (right) vs. temperature obtained for the reference and modified SOEC working under 1.3 V. Equilibrium values were marked as dashed line. Dashed lines are visual guides only.

above the thermodynamic equilibrium point, pointing out the role of electrochemical H_2O/CO_2 splitting with the further formation of CH_4 being independent of electrochemical reactions on the electrode. There are still several disputes over the impact of direct CO_2 electrolysis and rWGS on the final outcome of the SOEC [78]. In the case of these studies, it is believed that the modified electrode material is responsible for the increased CO_2 direct electrolysis in parallel to the rWGS reaction. The minor increase in the currents flowing through the electrolyte followed by the comparable CO yields, despite the higher CH_4 yields, is basic evidence for the aforementioned statement. The increased rate of CO_2 electrolysis on the surface of the electrode may be mostly due to the higher basicity and higher tendency to react with water to form oxy-hydroxides of the Co species compared to the NiO_x. This was predicted based on the high tendency of Co to undergo oxidation in a wet atmosphere and to further react the Co(O)OH species with CO_2 forming a corresponding metal carbonate. A series of reaction enthalpies and Gibbs energy changes (*Rea* module) were calculated and followed by the thermodynamic equilibrium composition (*Gem* module) simulation using HSC Chemistry for Ni and Co under the working SOEC idealized inlet gas mixture composition. The results of the simulations are presented in the Supplementary Materials (Figs. S3 and S4). The higher ability of Co to form oxides-hydroxides as well as adsorb and bond the CO_2 should increase the overall basicity of the electrode and increase the retention time of CO_2 on the surface [79]. This would result in two things: A) increase of the CO_2 electrolysis rate, and B) increase of the possibility of CO_2 hydrogenation to form CH_4 [80]. The obtained results prove the proposed mechanism of the increase in catalytic activity after Co addition. To develop the description of the routes leading to the enhanced efficiency of the Co-impregnated Ni-YSZ SOECs, a series of more sophisticated measurements were performed, and are discussed further in the text.

Electronic structure of modified cells and role of Co

To further examine the changes in the material properties after the introduction of the guest Co ions, a series of XAS and STXM measurements followed by a throughout spectra analysis with the assistance of the beamline specialists were performed at the SOLARIS synchrotron facility (Cracow, Poland). During the energy scans, the spectra for Ni-, Co-$L_{2,3}$ and O K absorption edges were collected for the as-prepared and spent samples. Due to the high amount of Ni in the base structure, the spectra of the Ni-$L_{2,3}$ edges were very similar for all of the samples with only slight evidence of Ni^{3+} forming on the surface after the tests (Figs. S5 and S6) [81]. The fluorescence signal was recognized as unreliable due to the strong self-absorption of Ni. A minor shift of the Ni edge and post-edge distortions may correspond to the formation of Ni–Co species. Much more reliable results with clear evidence of the electronic structure changes are presented in Fig. 5 in the form of $L_{2,3}$-edges of Co both in the total electron yield (TEY) and fluorescence (PFY) signal. To assist in the analysis, a series of certified reference materials were also subjected to the

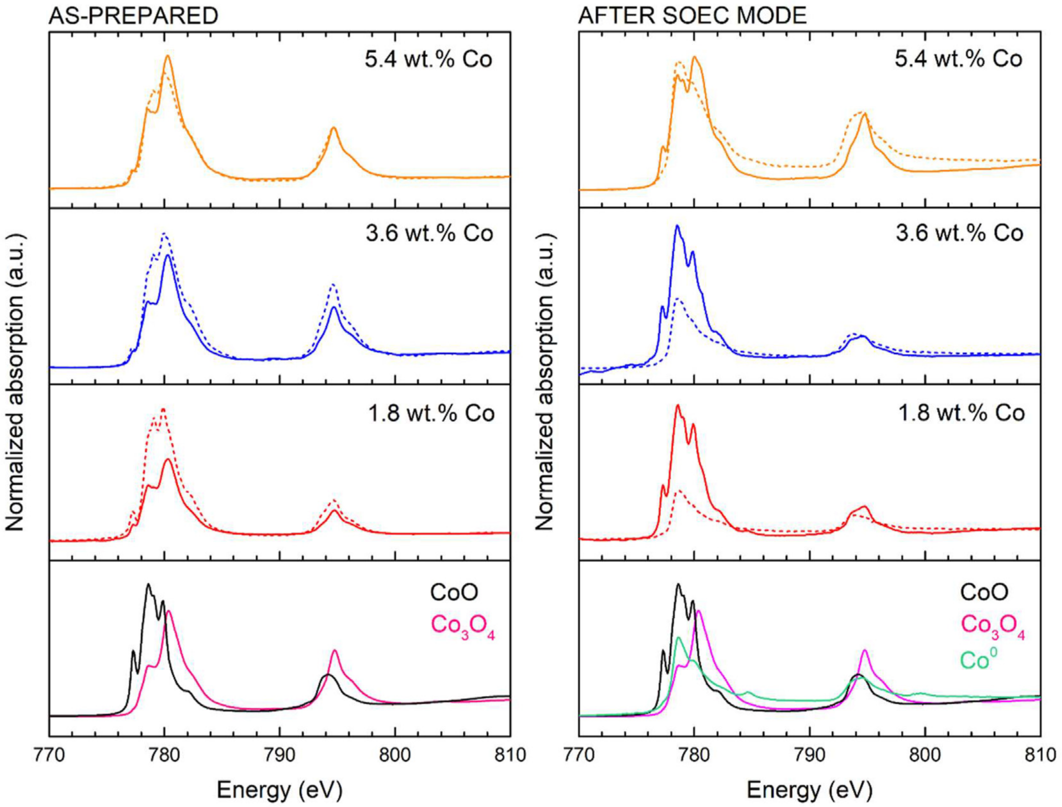

Fig. 5 – Co-$L_{2,3}$ absorption edge of Co-impregnated SOEC samples (left) as-prepared and (right) post-mortem – reduced after SOEC operation. TEY signal is represented as solid lines and PFY signal as dashed ones.

spectra collection. The XAS spectra are mostly dominated by the Co2p core-hole spin-orbit coupling, splitting the spectra into two regions – L_3, L_2 white lines parts. The changes in the shape of the absorption edge are clearly noticeable. The total TEY signal increased with the increase in the amount of Co in the structure. When taking the PFY signal as a reference point, it was observed that the ratio of the Co ions dissolved deeper into the oxide scale is higher for lower Co amounts. After repeated the impregnation steps, the intensity of both signals reached a ratio of ~1:1, showing that Co ions are much more likely to form surficial Co_xO_y oxides than to further dissolve into the NiO_x. This finding is in line with XPS results and analysis of the TEM images described previously. Disregarding the absorption intensity, the shape of the edges also slightly changed depending on the Co concentration. Looking at the reference spectra of CoO and Co_3O_4, there is a clear difference between the pre- and post-edge shape. The higher relative intensity and slight distortions of the pre-edge part, coming mostly from the CoO edge, can be easily observed in the case of the 1.8 wt% Co-impregnated sample. An even more pronounced difference in this region of the spectra can be seen in the PFY signal. As the Co concentration increased, its oxidation state slowly increased as the shape of the absorption edge started to very closely resemble that of Co_3O_4. According to research by Zhang B. et al., where the edge of the Co strongly resembled our result, it was stated that the Co^{2+}/Co^{3+} admixture varied around the 1:1 ratio [82]. Based on experimental and simulational research by Chang C.-F. et al., it was established that the created substructure of Co–Ni oxides contains mostly low spin Co^{3+} and high spin Co^{2+} ions [83]. The absorption edges of the samples after the SOEC testing revealed that the cobalt was reduced on the start-up procedure of the cell (resembling the Co^0 edge). Due to the presence of residual water vapor and noninert storage of the samples after the tests, a nanometric layer of the Co_xO_y oxide built up on the surface of the metal, with a higher share of Co_3O_4 in the case of the 5.4 wt% Co-impregnated sample. This indicated a lower stability and higher tendency of this sample to get oxidized, mostly due to the higher amount of initial free Co oxide species.

The O K absorption edges were measured and the results for the as-prepared 3.6 wt% Co-impregnated sample are presented in Fig. 6. The additional absorption edges of the reference materials were also included to resolve the composition of the surficial layer as the NiO, Co_3O_4, and $NiCo_2O_4$ compounds are characterized by slight shifts in the edge energy. The precise description of the pure $NiCo_2O_4$ preparation is detailed in the Supplementary Materials. Fortunately, the 8YSZ O K edge and the features coming from the carbon tape are located at an energy range that is not interfering with the shapes of the edges of Ni/Co-based compounds. Based on the obtained shape of the edge, three regions in superposition were highlighted and corresponded well with the placement of the absorption edges of the $NiCo_2O_4$, Co_3O_4, and NiO, respectively. The existence of the mixed Ni–Co spinel-like structure was identified based on the small pre-edge feature peaking at 529 eV, which indicated the existence of an increased share of Ni^{3+} ions in the surficial layer of the electrode [84]. The position of the Co edge pre-peak feature is also clearly visible and surely represents the Co_3O_4 nanoparticles formed within the spinel structure and on the surface of the 8YSZ ionic conductor.

The formation of $NiCo_2O_4$ increases the abundance of the Ni^{2+}/Ni^{3+} and Co^{2+}/Co^{3+} redox couples and through this can deliver a high number of active sites for performing chemical reactions. The recent studies focus on the use of $NiCo_2O_4$ normal and inverse spinel structure as the electrocatalyst. The position of the Ni and Co cations in the tetrahedral (T_d) or octahedral (O_h) sites determines the final performance of the catalyst [85]. The degree of the inversion in the Ni–Co spinel greatly changes the DOS and alters the electronic properties of the complex oxide. This further affects the SOEC performance as the purely reduced state is not most likely to happen. A high amount of water vapor increases the pO_2 and establishes an equilibrium between the formation and disintegration of the Ni–Co oxide mixed compound. It is generally agreed that the

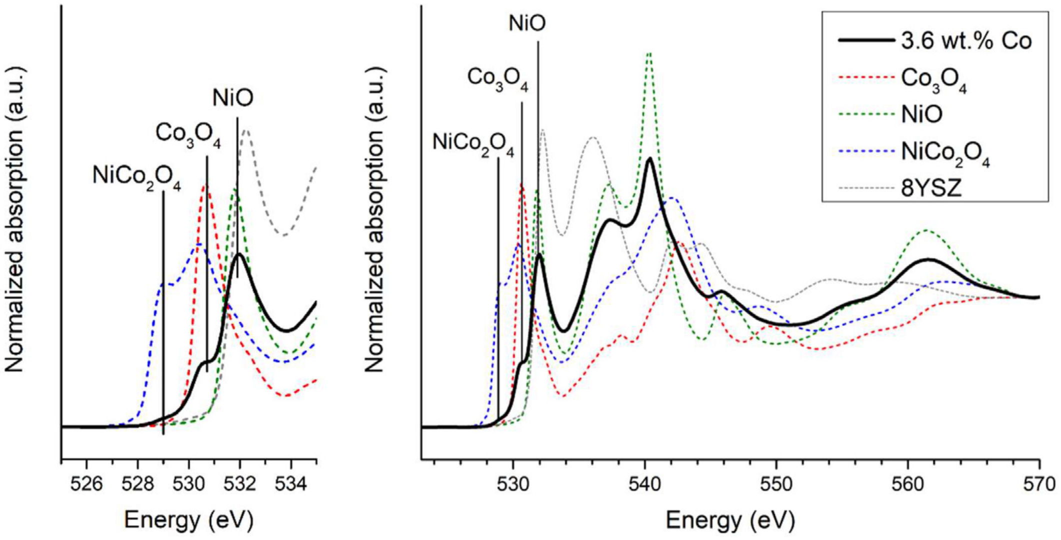

Fig. 6 – O K absorption edge of as-prepared 3.6 wt% Co-impregnated sample and reference materials.

existence of a high share of Ni^{3+} ions plays a crucial role in the electrochemical enhancement of the catalyst. The feature located at ~529 eV (Fig. 6) can be taken as newly appearing with the unoccupied e_g state of Ni^{3+} (3 d^7) hybridized with O2p [86,87]. Studies conducted by M. Cui et al. revealed that Co^{3+} located at T_d sites is thermodynamically unstable and tends to get reduced into the more stable Co^{2+} valence [88]. As a result of this change, the Ni^{2+} gets oxidized into Ni^{3+} to reach the charge neutrality of the lattice. It leads to the generation of a new hole state of Ni3d-character and shifting of the E_F closer to the valence band. The synergistic interaction between the Co and Ni may substantially increase the electronic conductivity and, in extreme cases, induce a metallic character of the $NiCo_2O_4$. The measurements at the O K edge can give a clear description of the interactions between the elements for the spinel-like structures that evolved in future samples.

To better represent the distribution of the elements regarding the properties of their electronic structure, a series of STXM images was collected. A representative set of the images of the as-prepared sample containing 3.6 wt% Co is presented in Fig. 7. This novel method of examination of the space distribution of the elements of the given absorption edge energy sheds new light on the results obtained during SEM imaging. Clear evidence was obtained of the above-mentioned statements regarding the formed structures of the Co-8YSZ facet and the Ni–Co intermixed oxide species. A reference scan performed much below the absorption edges of Ni and Co resembled the TEM image presented in Fig. 1. Elemental maps were obtained as the difference between the energy scan below and at the absorption edge. After reaching the energy of the Co-L_3 edge, the Co nanoparticles and $NiCo_2O_4$-like structure come up within the imaging region. Moving up to the higher scanning energy located at the Ni-L_3 edge, clear evidence of the bimodal state of the Ni was observed. The dark area is ascribed to the 8YSZ particle being impermeable to the radiation. The Co was homogeneously distributed over the sponge-like surficial structure of the reoxidized Ni particle, which indicates the presence of the $NiCo_2O_4$-like structure of reacted oxides. Additionally, not clearly visible in the TEM and SEM pictures, nanoparticles of Co_xO_y were identified both on the surface of the YSZ creating no obvious interlayer and as the inclusions of spherical nanoparticles embedded within the homogeneous structure of the mixed Ni–Co oxide. Minor bigger agglomerates were also noticed in the images, which indicated that the impregnation with the addition of βCD is a promising method for homogeneous modification of SOC cells. According to the Ni maps, the ions are found in the homogeneous surficial oxide scale. Interestingly, the formed structure resembles a core-shell particle where the internal part is mostly composed of metallic Ni (slight shift of the absorption edge). The gradient-like distribution of Ni ions beautifully revealed the layer-by-layer buildup of the structure where the metallic core is surrounded by a $NiCo_2O_4$-like structure and peripheral Co-enriched phase with Co_xO_y inclusions. The complex structure greatly represents the diffusion limitations of the Co ions, but at the same time brings more difficulties for the formulation of final conclusions regarding the primary reasons for the enhanced operation of the SOEC in co-electrolysis accompanied by methanation.

To better understand the interaction of Co and Ni species in the samples on start-up of the cell and reduction under flowing H_2, a series of H_2-TPR measurements were performed using our in-house-built TPx system. The corresponding reduction profiles are shown in Fig. 8. The reduction kinetics of all of the samples is beyond the obvious, as the process ends

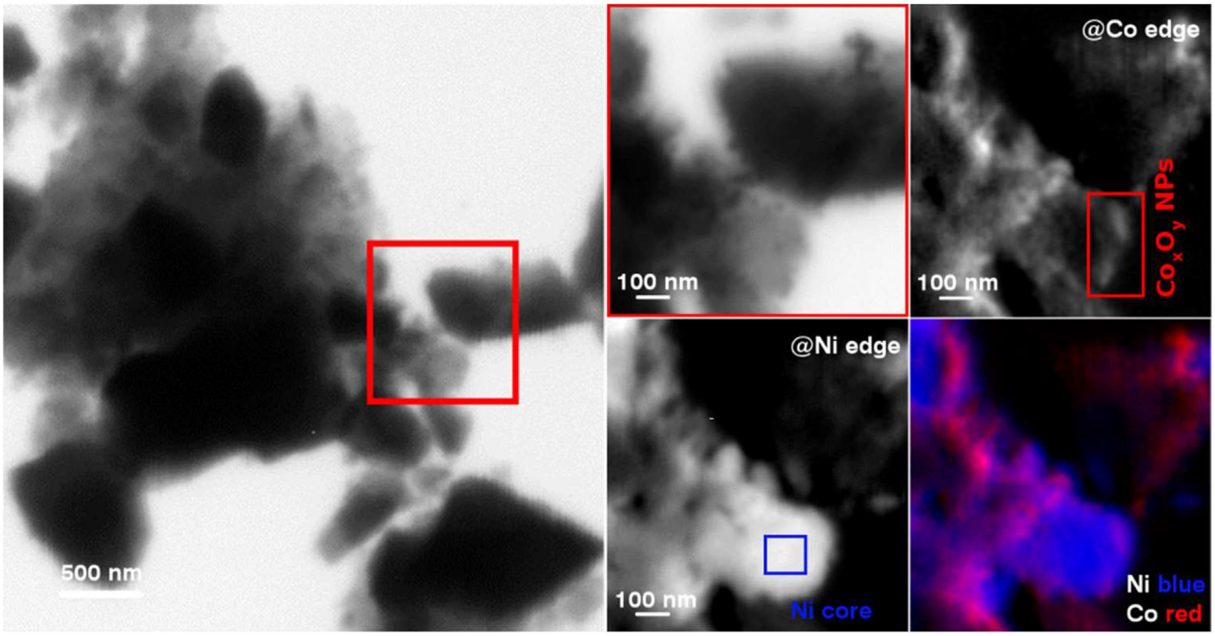

Fig. 7 – STXM images of the as-prepared 3.6 wt % Co-impregnated sample with the corresponding elemental distribution maps of Ni and Co. The Ni and Co map overlay is also presented.

much before 400 °C indicating the formation of the highly nanometric and porous structures which greatly reduce the reduction temperature. In general, for all of the samples, the shape of the reduction profile is composed of two distinctive regions, denoted as the lower temperature region (α) and higher temperature region (β). The first H_2 consumption peak (α) located at around 250 °C was related to the existence of the mesoporous surficial structure of paper ball-like oxide scale with an amorphous structure (see Fig. 1) as it is more likely to undergo fast oxygen uptake and release than the layers underneath. According to the literature and previous findings, the α peak can be attributed to the reduction of surface-active oxygen species adsorbed onto the surface of the mixed (Co,Ni) oxyhydroxides and/or smaller nanoparticles of (Ni,Co) oxides as the low temperature is sufficient to overcome the energy barrier of their release [89,90]. As a similar α peak appeared in the reference sample, it indicates a significant amount of Ni^{3+} ions, presumably both in the form of pure and Co-doped NiOOH. The low temperature during the sintering step of the prereduced samples under an ambient air atmosphere resulted in the formation of copious amounts of surficial oxyhydroxides of low crystallinity. This is in agreement with previously analyzed TEM images (Fig. 1).

The splitting of the β reduction peak, visible mostly for the 1.8 wt% Co-impregnated sample, is related to the coexistence of a $NiCo_2O_4$ spinel-like phase and embedded Co_xO_y nanoparticles. To better represent the deconvolution of the overlapping reduction processes, a series of H_2-TPR measurements was also performed for the 8YSZ particles impregnated with NiO, Co_3O_4, and $NiCo_2O_4$. The detailed procedure is included in Supplementary Materials and simulated the preparation steps covered in this research. The results are presented in Fig. 9. By comparison, it is clearly visible that the resultant H_2-TPR profile of the Co-containing cells is a superposition of the NiO-YSZ and Co_3O_4-YSZ reduction profiles and highly resembles the one of $NiCo_2O_4$-YSZ. The high-temperature β region was further deconvoluted into two subregions, namely β_1 and β_2. The first was attributed to the reduction of the NiO subphase being in strong interaction within Ni–Co spinel-like structure. Due to this interaction between the Ni and Co, the reduction temperature was significantly lower for the Co-impregnated samples. Based on research by Y. Yi et al., the reason for this shift is bidirectional [91]. Firstly, the synergistic effect of the coexistence of Ni–Co spinel-like compound facilitates the reaction between Ni^{3+} and Co^{2+} through the charge transfer reaction $Ni^{3+} + Co^{2+} \rightarrow Ni^{2+} + Co^{3+}$, which facilitates the easier reduction of Ni ions. The second reason is the higher dispersion of the NiO subphase throughout the whole structure and increased mesoporosity of the oxide scale after the introduction of Co. As in this research, the well-defined peak around 300 °C was attributed to the reduction of the bulk Ni^{2+} to Ni^0 based on the general data on the reduction behavior of nanometric NiO. The secondary process rising within the β_1 peak is the simultaneous reduction of Co^{3+} to Co^{2+} [92]. The β_1 was shown to undergo a slight shift towards higher temperatures, but still lower than for the unmodified sample. This indicates that the additional heating steps increase the crystallinity and average particle size of the scale.

The β_2 peak at around 340 °C was likened to the reduction of Co species. The position of the assigned process is also in

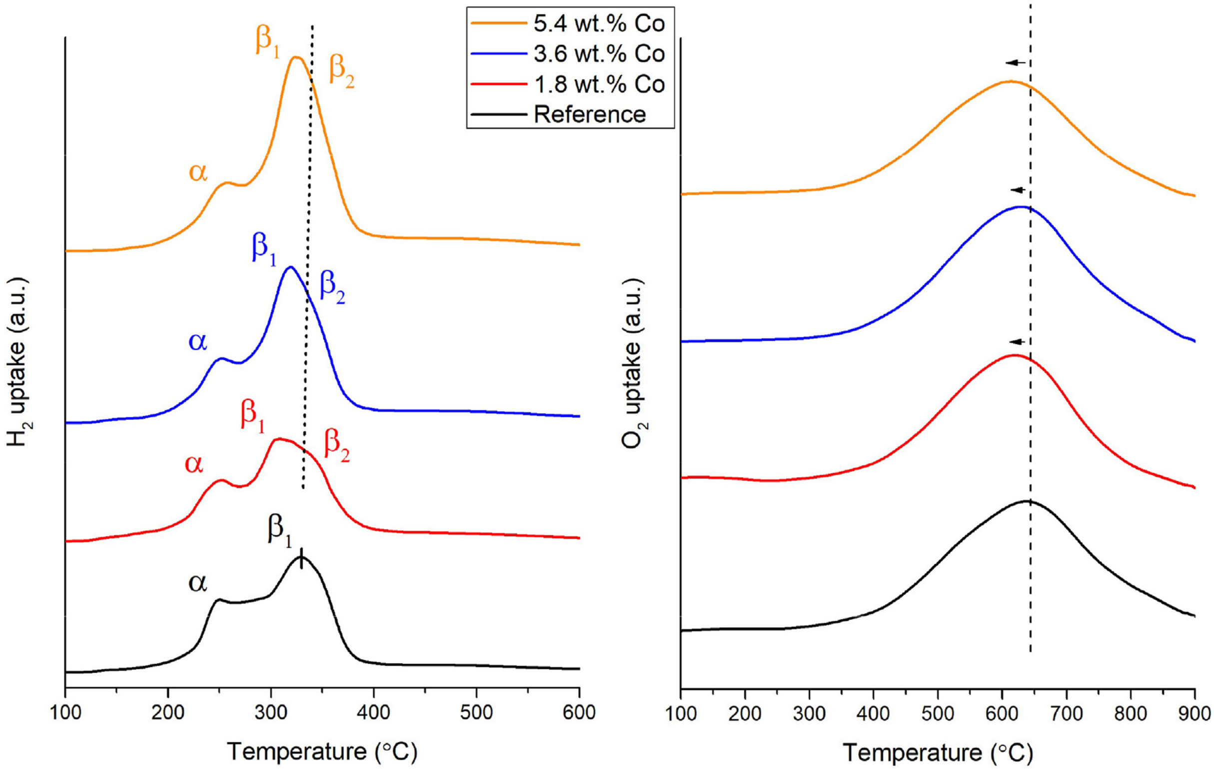

Fig. 8 – H_2-TPR (left) and O_2-TPO (right) profiles of the reference and Co-impregnated SOECs.

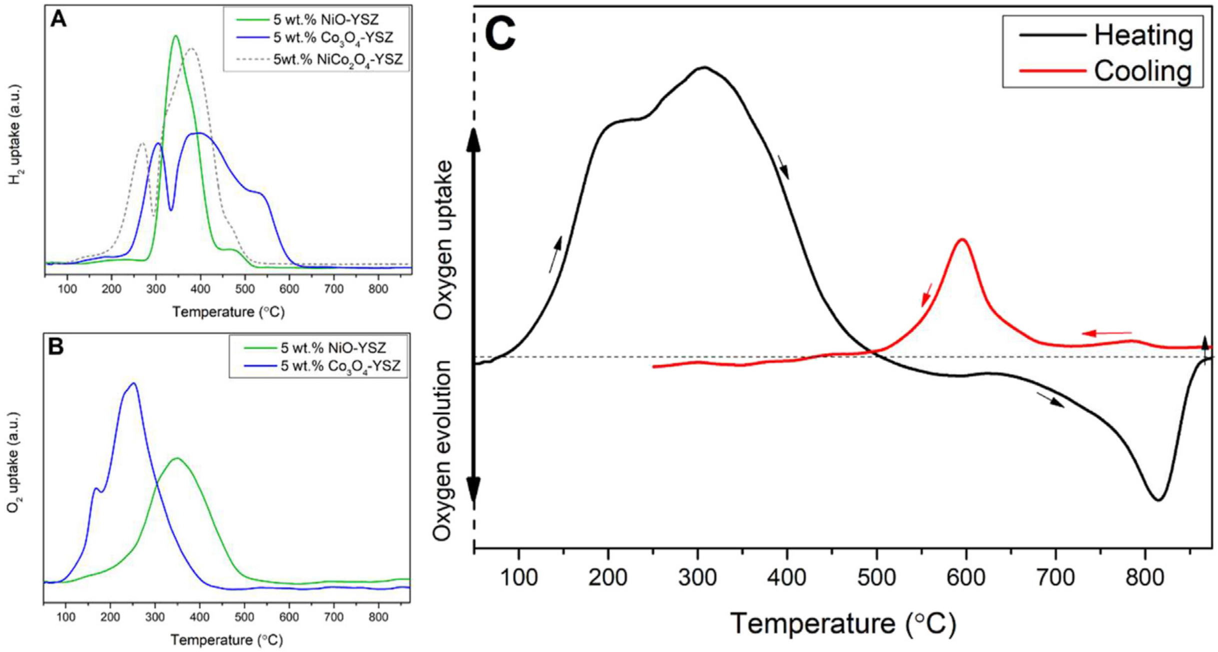

Fig. 9 – A) H_2-TPR profiles, B) O_2-TPO of NiO-YSZ and Co_3O_4-YSZ, and C) Cyclic O_2-TPO profile of the $NiCo_2O_4$-YSZ sample.

agreement with the profile of the Co_3O_4-YSZ reference material shown in Fig. 9. According to the findings of Niu J. et al. on $NiCo_2O_4$-based catalysts for toluene conversion at a temperature similar to that observed during this study, the reduction of Co^{2+} to metallic Co occurs [93]. Considering the reference material of Co_3O_4-YSZ, the main reduction peak of the aforementioned process was also shifted towards lower temperatures. The modified structure of the cells is hereby experiencing the synergistic effects of the mixing of the transition metals. On the one hand, the Co ions help to reduce the Ni ions at the lower temperature, while the metallic Ni speeds up the reduction of Co ions into the metallic form, most likely by the hydrogen spillover mechanism [94,95].

With the increasing number of impregnation steps, the β_1 and β_2 start to fully overlap each other, creating a profile that highly resembles that of the reference material $NiCo_2O_4$-YSZ (Fig. 9). This indicates that the abundance of the Co ions and longer diffusion time facilitated the formation of the proper Ni–Co mixed compound. For the 5.4 wt% Co-impregnated sample, the bimodal and enhanced reductivity are extinguished. It seems that the existence of the layer of lower crystallinity is of major importance.

O_2-TPO experiments were also performed to resolve the changes in the redox chemistry of the electrode due to the composition of the altered catalyst. The results of the measurements are presented in Fig. 8 and additional profiles of the reference materials are shown in Fig. 9. Agreeing with the Gibbs free energy calculations for the oxidation of Ni and Co metals and the TPO profiles presented in Fig. 9, the higher the amount of Co added into the electrode, the lower its oxidation temperature. This is direct evidence of the higher susceptibility of the modified material towards oxygen uptake. Taking into account that SOECs work under high water vapor pressures and the previous conclusions over the role of oxyhydroxides and Me^{3+}/Me^{2+} pairs, the higher ability to bind oxygen and form the surficial layer of the Ni–Co mixed oxide is of great importance for the final performance of the cell.

A novel behavior, previously undescribed in the literature, of the $NiCo_2O_4$-YSZ material was discovered and recorded. The behavior on reduction of the $NiCo_2O_4$-YSZ reference catalyst material was in line with other reports. Even so, the further O_2-TPO measurements revealed that the material, despite being subjected to the oxidizing atmosphere, was able to evolve additional oxygen from the lattice at elevated temperature (Fig. 9, right). A cyclic heating-cooling experiment was performed to ensure a reliable result. During the heating, the NiCo alloy supported on the YSZ substrate underwent full oxidation until ~450 °C. A further increase of the temperature over 600 °C caused the evolution of the oxygen from the catalyst material into the oxidant stream, even though it contained 5 vol% O_2 of He. This was recorded as a negative TCD detector signal. The cycle was completed with the cooling of the catalyst bed in the same stream of the gas mixture. On cooling, the process was fully reversed at around 600 °C again showing a positive TCD peak of a similar area. This interesting feature of the $NiCo_2O_4$ compound will be further studied to understand the chemical and physical causes of the discovery. The primary hypotheses are threefold. The first states that the compound disintegrates into two major compounds – NiO and CoO – with the simultaneous release of the redundant oxygen. The second covers the issues concerning the change of the crystallographic structure of the spinel. And finally, the most promising one: the reduction on oxidation may directly correspond to the oxygen activity coefficient and oxygen bond strength. When subjected to a slightly oxygen-depleted atmosphere, the lower pO_2 causes the partial reduction of the surface of the spinel causing the kinetics of the lattice oxygen release to overedge the kinetics of oxygen uptake. The results of those analyses will be of significant scientific value to the field of materials science and catalysis. Furthermore, according to this research, the behavior of the spinel structure may explain the increased catalytic activity of the electrode after the introduction of Co. The increase in the oxygen exchange rate should highly influence especially the electrocatalytic activity in the context of water splitting in the SOEC.

Performance under altered voltage and CO_2/H_2 ratio

To better illustrate the dependencies between the actual inlet mixture composition and the final output of the SOEC, a series of tests under various H_2/CO_2 ratios and operating voltages were performed. The results are presented in Fig. 10A–C. The representative temperature of 640 °C and the 3.6 wt% Co-impregnated sample were chosen for all tests. When the influence of voltage changes was examined, the inlet mixture was set to 2:1 H_2 to CO_2, and for the mixture change-related test, a thermoneutral bias of 1.3 V was selected. While increasing the bias applied to the SOEC, the CH_4 concentration increased linearly, followed by a similar trend observed for the CO concentration (Fig. 10A). Due to the increased conversion, the corresponding concentration of CO_2 dropped in the same manner. Despite this, the cell maintained the same linear dependence of the current increase with the increase in voltage (Fig. S7). This indicates that the cell performed well, even though a relatively low temperature was maintained. The increase in the CH_4 concentration was a result of the shifting of the thermodynamic equilibrium by increasing the amount of the reactants – mainly CO and H_2 – which enabled the high rates of the methanation. When changing the H_2/CO_2 vol. ratio at a fixed bias (1.3 V), an increase in the CH_4 concentration was observed until the 4:1 vol ratio was reached. After that point, the CH_4 yield remained almost unchanged due to the highly depleted carbon source for the methanation reaction to happen. An interesting view of the electrochemical aspects of

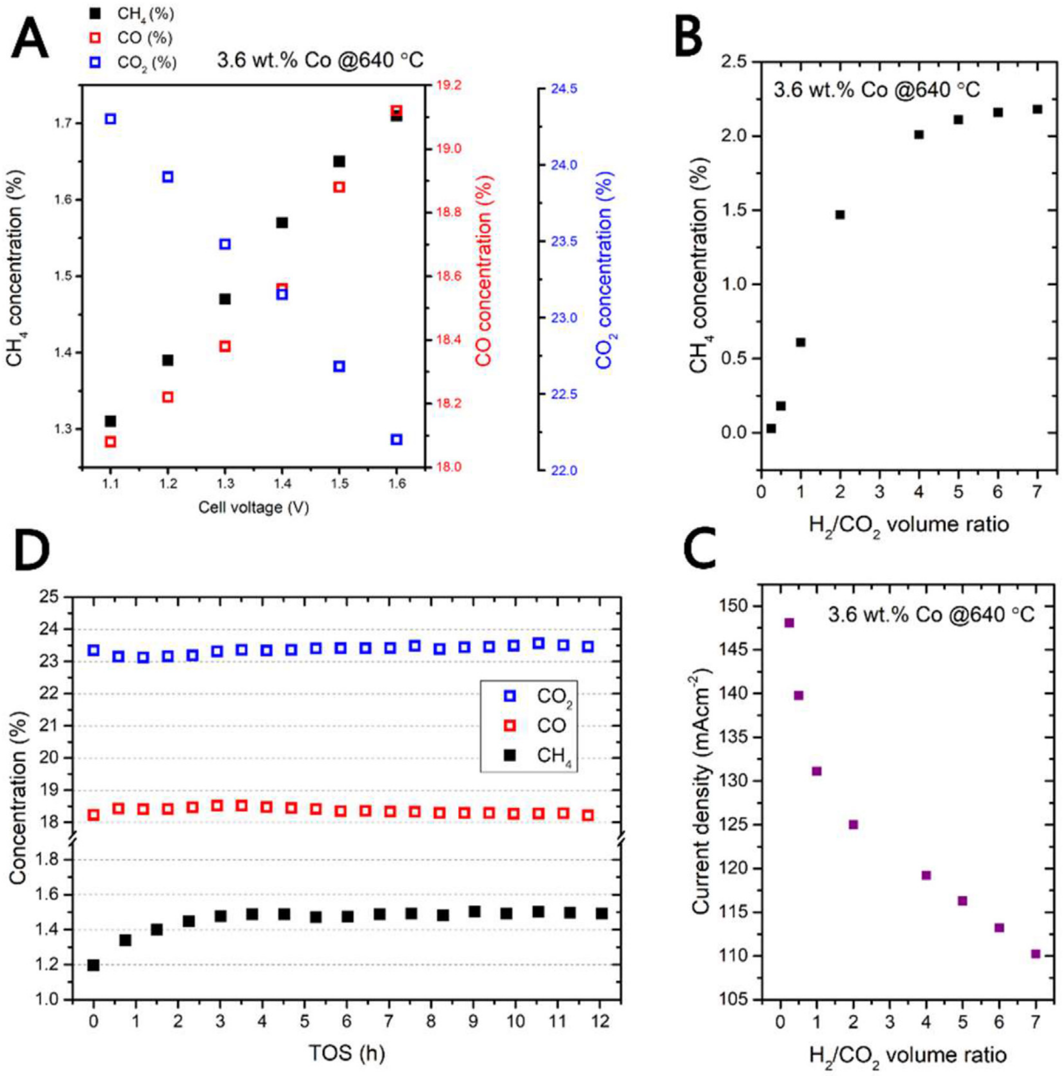

Fig. 10 – **Performance tests of the 3.6 wt% Co-impregnated sample. A) change of the outlet gas concentrations vs. cell voltage, B–C) change of CH_4 concentration and current density vs. H_2/CO_2 inlet mixture vol. ratio, and D) 12 h Time-On-Stream measurements in SOEC mode.**

the work of the SOEC was seen when the change of the CH_4 in the outlet stream (Fig. 10B) and the current change (Fig. 10C) were compared. After the increase of the share of H_2 in the inlet mixture, the CH_4 easily reached the thermodynamic equilibrium concentration while the current flowing through the SOEC kept decreasing. The fixed amount of H_2O vapor followed by the decreasing share of CO_2 limited the electrolysis efficiency due to the lack of reactants to be reduced. This is proof that the CO_2 can also be directly electroreduced on the electrode material, in parallel to the fast, ongoing rWGS reaction.

To better represent the stability of the SOEC with additional modifications, a prolonged test for 12 h was carried out. The cell was subjected to the same start-up procedure and after the gas switch to the H_2/CO_2 mixture, the concentration changes were monitored every 15 min. The Time-On-Stream measurements are shown in Fig. 10D. The results gave us clear evidence that the Co impregnation does not change the stability of the pristine cell, while increasing the catalytic activity and maintaining its performance for over 12 h. During the first hours of electrolysis, a slight decrease was observed mostly due to Ni particle growth and sintering. This is a normal behavior for SOCs, and after a few hours the CH_4 concentration remained nearly unchanged. A similar trend was noticed for the CO and CO_2 concentration changes, where after 6 h of testing, the value oscillated around 18% and 23.5%, respectively. This shows that the introduction of Co into the structure enormously enhances the catalytic performance with no negative impact on the cell stability issues.

Post-mortem imaging was done to observe the structural changes after reduction and 12 h of operation in SOEC mode. The SEM and TEM images of the spent electrodes are depicted in Fig. 11. An additional collection of elemental maps using μEDS was performed for the 3.6 wt% Co-impregnated sample. After the reduction step, the Ni and Co got fully reduced and the bimetallic alloy formed on the surface of the Ni particles. The Ni grains looked homogeneous and no clear evidence of the formation of secondary phases was found. This is due to an interesting aspect of the binary Ni–Co phase diagram, which states that both elements can form solid solutions throughout the whole range of concentrations, due to their close proximity on the periodic table and similar atomic structures [96,97]. In contrast, the Co in its metallic form created a distinctive structure of spherical nanoparticles on the 8YSZ grains. It demonstrates nearly no solubility of the Co in 8YSZ with the tendency of the metal to undergo dewetting and form a network of homogeneous nanoparticles. This is true in the case of the 1.8, and 3.6 wt% Co-impregnated samples, while for the 5.4 wt% Co-impregnated sample the amount of Co was so significant that a strong agglomeration process occurred. Also, a higher tendency towards oxidation led to the possible formation of the secondary flake-like phase visible in Fig. 11. Based on the previous XAS measurements, it may be composed of cobalt oxides that were prereduced and not fully dissolved into the Ni matrix, further oxidized during the cell cooldown scheme. The highest homogeneity was assigned to the sample containing 3.6 wt% Co in the structure. The TEM images and elemental maps are in line with the

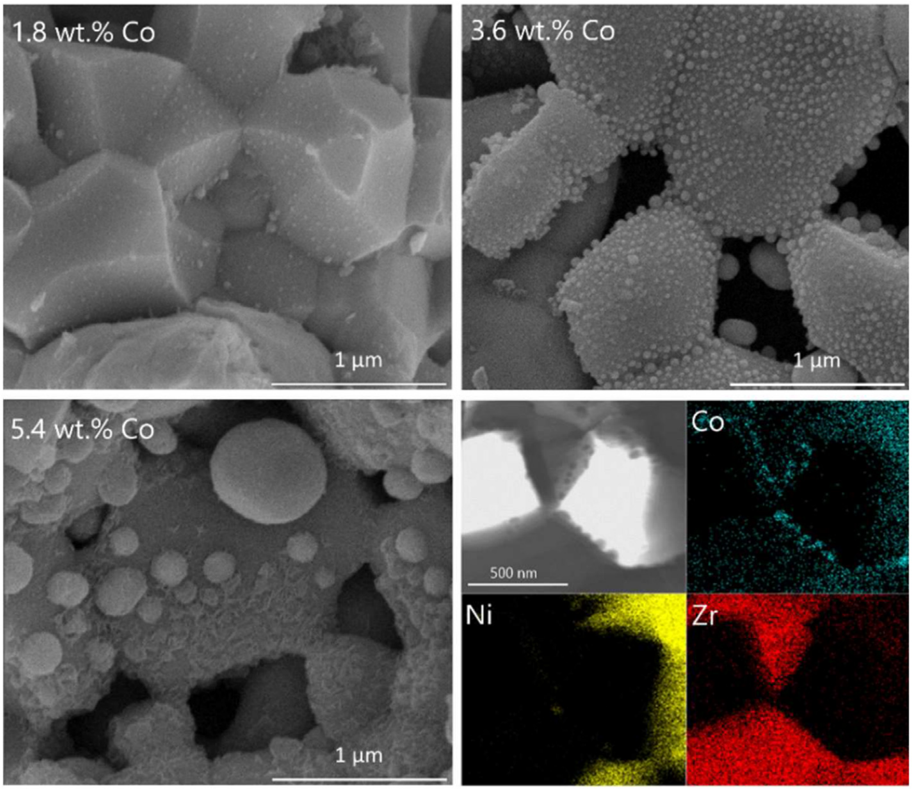

Fig. 11 – SEM images of the spent electrodes and TEM image of 3.6 wt% Co-impregnated sample with corresponding elemental maps.

aforementioned analysis showing the Ni–Co homogeneous mixture and Co nanoparticles anchored to the surface of the 8YSZ. As to the cell's performance, the existence of both the Co-YSZ system resulting in higher basicity, and $NiCo_2O_4$ spinel-like oxide for providing active sites and the increase in specific surface area can be ascribed as the major causes of its enhancement.

Conclusions

The purpose of this work was to successfully modify conventional Solid Oxide Electrolysis Cells via Co-impregnation and characterize the changes it caused to the internal microstructure, phase composition, and electronic structure in detail. The modifications consisted of the introduction of small amounts of Co into the Ni-YSZ cermet material of the cells via the wet impregnation method. The addition of βCD resulted in the homogeneous dispersion of the Co ions throughout the material bulk. It was observed that the Co ions formed three types of substructures, namely nanoparticles of Co_xO_y supported on the surface of the 8YSZ, Ni–Co mixed spinel-like compound on the interface between the Ni core and outer layer, and Co_xO_y nanoparticles embedded into the spinel scale. The XPS results indicated that Co induced the formation of a high amount of Ni^{3+} ions. This directly increased the number of the available catalytic sites through the active Ni^{3+}/Ni^{2+} and Co^{3+}/Co^{2+} couples for reactions to happen. The performed modifications increased the CH_4 concentration in the outlet stream over 2.5 times and ensured better efficiency of the H_2O/CO_2 co-electrolysis and conversion. The addition of Co increased the CO_2 conversion from 47% up to 57% at 700 °C. The search for the possible causes of the enhancement through XAS and STXM measurements resulted in direct proof of the existence of a significant amount of the intermixed Ni–Co compound which induced changes in the shift of the E_F band energy, generated the inverse spinel structure, and introduced a significant amount of active surface species. The STXM measurements clearly evidenced a Co-graduated structure of core-shell-like Ni grains. The H_2-TPR and O_2-TPO studies revealed that highly developed and nanometric structures were formed after the Co introduction. The modified cells were characterized by a lower reduction temperature due to the synergistic effects of the coexistence of Ni and Co. A highly novel discovery concerning the interesting behavior of the $NiCo_2O_4$ supported on the 8YSZ was made. Even though the TPO experiment was carried out in an oxidizing atmosphere, the powder evolved additional oxygen at high temperatures, only to reverse this process when cooling down. Tests under various operating voltages and H_2/CO_2 inlet ratios led to the general proof of simultaneous direct and indirect (rWGS) routes of CO_2 electroreduction. The 3.6 wt% Co-impregnated sample was characterized by the most homogeneous distribution of Co species across the cermet material and small, spherical nanoparticles developed within the structure. The addition of the secondary metal into the Ni-YSZ conventional cermet material revealed highly promising results to be further applied in the field of H_2O/CO_2 co-electrolysis with the simultaneous single-process of methanation for the buildup of advanced conversion systems. Further studies on the bimetallic synergy and strange spinel behavior under different pO_2 and elevated temperatures are planned to better understand the phenomena.

Declaration of competing interest

The authors declare that they have no known competing financial interests or personal relationships that could have appeared to influence the work reported in this paper.

Acknowledgements

This work was supported by the 5th Polish-Taiwanese/Taiwanese-Polish Joint Research Project PL-TW/V/4/2018 granted by the National Centre for Research and Development of Poland and the Ministry of Science and Technology of Taiwan. This publication was developed under the provision of the Polish Ministry of Education and Science project: "Support for research and development with the use of research infrastructure of the National Synchrotron Radiation Centre SOLARIS" under contract nr 1/SOL/2021/2. We acknowledge SOLARIS Centre for the access to the Beamline PIRX and Beamline DEMETER, where the measurements were performed.

Appendix A. Supplementary data

Supplementary data to this article can be found online at https://doi.org/10.1016/j.ijhydene.2022.08.057.

REFERENCES

[1] Wang X, Zhu L, Zhuo Y, Zhu Y, Wang S. Enhancement of CO2 methanation over La-modified Ni/SBA-15 catalysts prepared by different doping methods. ACS Sustainable Chem Eng 2019;7:14647–60. https://doi.org/10.1021/acssuschemeng.9b02563.

[2] Chen Wei-Yin, Seiner John, Toshio Suzuki ML. Handbook of climate change mitigation and adaptation. 2nd ed., vol. 3; 2016. https://doi.org/10.1007/978-3-319-14409-2_39.

[3] Jiang Y, Chen F, Xia C. A review on cathode processes and materials for electro-reduction of carbon dioxide in solid oxide electrolysis cells. J Power Sources 2021:493. https://doi.org/10.1016/J.JPOWSOUR.2021.229713.

[4] Chen X, Guan C, Xiao G, Du X, Wang JQ. Syngas production by high temperature steam/CO2 coelectrolysis using solid oxide electrolysis cells. Faraday Discuss 2015;182:341–51. https://doi.org/10.1039/c5fd00017c.

[5] Wang Y, Liu T, Lei L, Chen F. High temperature solid oxide H2O/CO2 co-electrolysis for syngas production. Fuel Process Technol 2017;161:248–58. https://doi.org/10.1016/j.fuproc.2016.08.009.

[6] Ioannidou E, Neophytides S, Niakolas DK. Experimental clarification of the RWGS reaction effect in H2O/CO2 SOEC Co-electrolysis conditions. Catalyst 2019;9:151. https://doi.org/10.3390/CATAL9020151. 2019;9:151.

[7] Mahmood A, Bano S, Yu JH, Lee KH. Effect of operating conditions on the performance of solid electrolyte

membrane reactor for steam and CO2 electrolysis. J Membr Sci 2015;473:8–15. https://doi.org/10.1016/J.MEMSCI.2014.09.002.

[8] Ebbesen SD, Graves C, Mogensen M. Production of synthetic fuels by Co-electrolysis of steam and carbon dioxide, vol. 6; 2009. p. 646. https://doi.org/10.1080/15435070903372577. 60.

[9] Kim-Lohsoontorn P, Bae J. Electrochemical performance of solid oxide electrolysis cell electrodes under high-temperature coelectrolysis of steam and carbon dioxide. J Power Sources 2011;196:7161–8. https://doi.org/10.1016/J.JPOWSOUR.2010.09.018.

[10] Stoots C, O'Brien J, Hartvigsen J. Results of recent high temperature coelectrolysis studies at the Idaho National Laboratory. Int J Hydrogen Energy 2009;34:4208–15. https://doi.org/10.1016/J.IJHYDENE.2008.08.029.

[11] Zhan Z, Zhao L. Electrochemical reduction of CO2 in solid oxide electrolysis cells. J Power Sources 2010;195:7250–4. https://doi.org/10.1016/J.JPOWSOUR.2010.05.037.

[12] Liang J, Han M. Different performance and mechanisms of CO2 electrolysis with CO and H2 as protective gases in solid oxide electrolysis cell. Int J Hydrogen Energy 2022;47:18606–18. https://doi.org/10.1016/j.ijhydene.2022.04.061. https://doi.org.

[13] Xi C, Sang J, Wu A, Yang J, Qi X, Guan W, et al. Electrochemical performance and durability of flat-tube solid oxide electrolysis cells for H2O/CO2 co-electrolysis. Int J Hydrogen Energy 2022;47:10166–74. https://doi.org/10.1016/j.ijhydene.2022.01.105. https://doi.org.

[14] Zheng Y, Chen Z, Zhang J. Solid oxide electrolysis of H2O and CO2 to produce hydrogen and low-carbon fuels. Electrochem Energy Rev 2021;4:508–17. https://doi.org/10.1007/s41918-021-00097-4.

[15] Liu C, Sun C, Bian L, Yu W, Qi J, Li S, et al. Robust Ni-doped Ruddlesden-popper (La,Sr)Fe1-xNixO4+δ oxide as solid oxide cells fuel electrode for CO2 electrolysis. Int J Hydrogen Energy 2022;47:9517–26. https://doi.org/10.1016/j.ijhydene.2022.01.054. https://doi.org.

[16] Zheng Y, Wang S, Pan Z, Yin B. Electrochemical CO2 reduction to CO using solid oxide electrolysis cells with high-performance Ta-doped bismuth strontium ferrite air electrode. Energy 2021;228:120579. https://doi.org/10.1016/j.energy.2021.120579. https://doi.org.

[17] Shen L, Xu J, Zhu M, Han YF. Essential role of the support for nickel-based CO2 methanation catalysts. ACS Catal 2020;10:14581–91. https://doi.org/10.1021/acscatal.0c03471.

[18] Wang W, Gong J. Methanation of carbon dioxide: an overview. Front Chem Eng China 2011;5:2–10. https://doi.org/10.1007/s11705-010-0528-3.

[19] Kazempoor P, Asadi J, Braun RJ. Validation challenges in solid oxide electrolysis cell modeling fueled by low Steam/CO2 ratio. Int J Hydrogen Energy 2022;47:15952. https://doi.org/10.1016/j.ijhydene.2022.03.115. –9. https://doi.org.

[20] Le Saché E, Pastor-Pérez L, Haycock BJ, Villora-Picó JJ, Sepúlveda-Escribano A, Reina TR. Switchable catalysts for chemical CO2 recycling: a step forward in the methanation and reverse water-gas shift reactions. ACS Sustainable Chem Eng 2020;8:4614–22. https://doi.org/10.1021/acssuschemeng.0c00551.

[21] Tsiotsias AI, Charisiou ND, Yentekakis IV, Goula MA. Bimetallic Ni-based catalysts for CO2 methanation: a review. Nanomaterials 2021;11:1–34. https://doi.org/10.3390/nano11010028.

[22] Alrafei B, Polaert I, Ledoux A, Azzolina-Jury F. Remarkably stable and efficient Ni and Ni-Co catalysts for CO2 methanation. Catal Today 2020;346:23–33. https://doi.org/10.1016/j.cattod.2019.03.026.

[23] Hatta AH, Jalil AA, Hassan NS, Hamid MYS, Rahman AFA, Teh LP, et al. A review on recent bimetallic catalyst development for synthetic natural gas production via CO methanation. Int J Hydrogen Energy 2021. https://doi.org/10.1016/j.ijhydene.2021.10.213.

[24] Gao J, Wang Y, Ping Y, Hu D, Xu G, Gu F, et al. A thermodynamic analysis of methanation reactions of carbon oxides for the production of synthetic natural gas. RSC Adv 2012;2:2358–68. https://doi.org/10.1039/C2RA00632D.

[25] Lv C, Xu L, Chen M, Cui Y, Wen X, Li Y, et al. Recent progresses in constructing the highly efficient Ni based catalysts with advanced low-temperature activity toward CO2 methanation. Front Chem 2020;8:269. https://doi.org/10.3389/FCHEM.2020.00269/BIBTEX.

[26] Lee WJ, Li C, Prajitno H, Yoo J, Patel J, Yang Y, et al. Recent trend in thermal catalytic low temperature CO2 methanation: a critical review. Catal Today 2021;368:2–19. https://doi.org/10.1016/j.cattod.2020.02.017.

[27] Younas M, Leong †, Kong L, Bashir MJK, Nadeem H, Shehzad A, et al. Recent advancements, fundamental challenges, and opportunities in catalytic methanation of CO 2 2016. https://doi.org/10.1021/acs.energyfuels.6b01723.

[28] Nizio M, Albarazi A, Cavadias S, Amouroux J, Galvez ME, Da Costa P. Hybrid plasma-catalytic methanation of CO2at low temperature over ceria zirconia supported Ni catalysts. Int J Hydrogen Energy 2016;41:11584–92. https://doi.org/10.1016/J.IJHYDENE.2016.02.020.

[29] Liu H, Xu S, Zhou G, Xiong K, Jiao Z, Wang S. CO2 hydrogenation to methane over Co/KIT-6 catalysts: effect of Co content. Fuel 2018;217:570–6. https://doi.org/10.1016/J.FUEL.2017.12.112.

[30] Czekaj I, Loviat F, Raimondi F, Wambach J, Biollaz S, Wokaun A. Characterization of surface processes at the Ni-based catalyst during the methanation of biomass-derived synthesis gas: X-ray photoelectron spectroscopy (XPS). Appl Catal Gen 2007;329:68–78. https://doi.org/10.1016/J.APCATA.2007.06.027.

[31] Tao M, Meng X, Lv Y, Bian Z, Xin Z. Effect of impregnation solvent on Ni dispersion and catalytic properties of Ni/SBA-15 for CO methanation reaction. Fuel 2016;165:289–97. https://doi.org/10.1016/J.FUEL.2015.10.023.

[32] De S, Zhang J, Luque R, Yan N. Ni-based bimetallic heterogeneous catalysts for energy and environmental applications. Energy Environ Sci 2016;9:3314–47. https://doi.org/10.1039/C6EE02002J.

[33] Falbo L, Visconti CG, Lietti L, Szanyi J. The effect of CO on CO2 methanation over Ru/Al2O3 catalysts: a combined steady-state reactivity and transient DRIFT spectroscopy study. Appl Catal B Environ 2019;256:117791. https://doi.org/10.1016/J.APCATB.2019.117791.

[34] Rönsch S, Schneider J, Matthischke S, Schlüter M, Götz M, Lefebvre J, et al. Review on methanation – from fundamentals to current projects. Fuel 2016;166:276–96. https://doi.org/10.1016/J.FUEL.2015.10.111.

[35] Liu P, Zhao B, Li S, Shi H, Ma M, Lu J, et al. Influence of the microstructure of Ni-Co bimetallic catalyst on CO methanation. Ind Eng Chem Res 2020;59:1845–54. https://doi.org/10.1021/acs.iecr.9b05951.

[36] Giorgianni G, Mebrahtu C, Schuster ME, Large AI, Held G, Ferrer P, et al. Elucidating the mechanism of the CO2methanation reaction over Ni-Fe hydrotalcite-derived catalysts: via surface-sensitive in situ XPS and NEXAFS. Phys Chem Chem Phys 2020;22:18788–97. https://doi.org/10.1039/D0CP00622J.

[37] Mebrahtu C, Krebs F, Perathoner S, Abate S, Centi G, Palkovits R. Hydrotalcite based Ni-Fe/(Mg, Al)O:X catalysts for CO2 methanation-tailoring Fe content for improved CO dissociation, basicity, and particle size. Catal Sci Technol 2018;8:1016–27. https://doi.org/10.1039/C7CY02099F.

[38] Pandey D, Deo G. Promotional effects in alumina and silica supported bimetallic Ni–Fe catalysts during CO2 hydrogenation. J Mol Catal Chem 2014;382:23–30. https://doi.org/10.1016/J.MOLCATA.2013.10.022.

[39] Serrer MA, Kalz KF, Saraçi E, Lichtenberg H, Grunwaldt JD. Role of iron on the structure and stability of Ni3.2Fe/Al2O3 during dynamic CO2 methanation for P2X applications. ChemCatChem 2019;11:5018–21. https://doi.org/10.1002/CCTC.201901425.

[40] Guo M, Lu G. The regulating effects of cobalt addition on the catalytic properties of silica-supported Ni–Co bimetallic catalysts for CO2 methanation. React Kinet Mech Catal 2014;113:101–13. https://doi.org/10.1007/S11144-014-0732-0.

[41] Jia C, Dai Y, Yang Y, Chew JW. Nickel-cobalt catalyst supported on TiO2-coated SiO2 spheres for CO2 methanation in a fluidized bed. Int J Hydrogen Energy 2019;44:13443–55. https://doi.org/10.1016/J.IJHYDENE.2019.04.009.

[42] Xu L, Lian X, Chen M, Cui Y, Wang F, Li W, et al. CO2 methanation over Co–Ni bimetal-doped ordered mesoporous Al2O3 catalysts with enhanced low-temperature activities. Int J Hydrogen Energy 2018;43:17172–84. https://doi.org/10.1016/J.IJHYDENE.2018.07.106.

[43] Jeong HY, Kim SW, Bae Y, Yoon KJ, Lee JH, Hong J. Effect of Fe infiltration to Ni/YSZ solid-oxide-cell fuel electrode on steam/CO2 co-electrolysis. Int J Energy Res 2019;43:4949–58. https://doi.org/10.1002/er.4577.

[44] Bai L, Wyrwalski F, Lamonier JF, Khodakov AY, Monflier E, Ponchel A. Effects of β-cyclodextrin introduction to zirconia supported-cobalt oxide catalysts: from molecule-ion associations to complete oxidation of formaldehyde. Appl Catal B Environ 2013;138–139:381–90. https://doi.org/10.1016/j.apcatb.2013.03.015.

[45] Zając M, Giela T, Freindl K, Kollbek K, Korecki J, Madej E, et al. The first experimental results from the 04BM (PEEM/XAS) beamline at Solaris. Nucl Instrum Methods Phys Res Sect B Beam Interact Mater Atoms 2021;492:43–8. https://doi.org/10.1016/j.nimb.2020.12.024. https://doi.org.

[46] Chlipała M, Błaszczak P, Wang SF, Jasiński P, Bochentyn B. In situ study of a composition of outlet gases from biogas fuelled Solid Oxide Fuel Cell performed by the Fourier Transform Infrared Spectroscopy. Int J Hydrogen Energy 2019;44:13864–74. https://doi.org/10.1016/j.ijhydene.2019.03.243.

[47] Menges F. Spectragryph - optical spectroscopy software. 2021., Version 1.2.15. http://www.effemm2.de/spectragryph/.

[48] Han L, Meng Q, Wang D, Zhu Y, Wang J, Du X, et al. Interrogation of bimetallic particle oxidation in three dimensions at the nanoscale. Nat Commun 2016;7:1–9. https://doi.org/10.1038/ncomms13335.

[49] Gonçalves JM, Silva MNT, Naik KK, Martins PR, Rocha DP, Nossol E, et al. Multifunctional spinel MnCo2O4based materials for energy storage and conversion: a review on emerging trends, recent developments and future perspectives. J Mater Chem 2021;9:3095–124. https://doi.org/10.1039/d0ta11129e.

[50] Zhao X, Mao L, Cheng Q, Li J, Liao F, Yang G, et al. Two-dimensional spinel structured Co-based materials for high performance supercapacitors: a critical review. Chem Eng J 2020;387:124081. https://doi.org/10.1016/j.cej.2020.124081.

[51] Lankauf K, Cysewska K, Karczewski J, Mielewczyk-Gryń A, Górnicka K, Cempura G, et al. MnxCo3-xO4 spinel oxides as efficient oxygen evolution reaction catalysts in alkaline media. Int J Hydrogen Energy 2020;45:14867–79. https://doi.org/10.1016/j.ijhydene.2020.03.188.

[52] Son JM, Oh S, Bae SH, Nam S, Oh IK. A pair of NiCo 2 O 4 and V 2 O 5 nanowires directly grown on carbon fabric for highly bendable lithium-ion batteries. Adv Energy Mater 2019;9:1–10. https://doi.org/10.1002/aenm.201900477.

[53] Zhang T, Yang K, Wang C, Li S, Zhang Q, Chang X, et al. Nanometric Ni5P4 clusters nested on NiCo2O4 for efficient hydrogen production via alkaline water electrolysis. Adv Energy Mater 2018;8:2–7. https://doi.org/10.1002/aenm.201801690.

[54] Zhong L, Kropp T, Baaziz W, Ersen O, Teschner D, Schlögl R, et al. Correlation between reactivity and oxidation state of cobalt oxide catalysts for CO preferential oxidation. ACS Catal 2019;9:8325–36. https://doi.org/10.1021/acscatal.9b02582.

[55] Błaszczak P, Mizera A, Bochentyn B, Wang S-F, Jasiński P. Preparation of methanation catalysts for high temperature SOEC by β-cyclodextrin-assisted impregnation of nano-CeO2 with transition metal oxides. Int J Hydrogen Energy 2021. https://doi.org/10.1016/j.ijhydene.2021.10.144.

[56] Huang L, Zhang W, Xiang J, Xu H, Li G, Huang Y. Hierarchical core-shell NiCo 2 O 4 @NiMoO 4 nanowires grown on carbon cloth as integrated electrode for high-performance supercapacitors. Sci Rep 2016;6:1–8. https://doi.org/10.1038/srep31465.

[57] Cetin A, Esenturk EN. Hierarchical nanowire and nanoplate-assembled NiCo2O4–NiO biphasic microspheres as effective electrocatalysts for oxygen evolution reaction. Mater Today Chem 2019;14:100215. https://doi.org/10.1016/j.mtchem.2019.100215.

[58] Dai X, Dai Y, Lu J, Pu L, Wang W, Jin J, et al. Cobalt oxide nanocomposites modified by NiCo-layered double hydroxide nanosheets as advanced electrodes for supercapacitors. Ionics 2020;26:2501–11. https://doi.org/10.1007/s11581-019-03333-6.

[59] Lai C, Wang Y, Fu L, Song H, Liu B, Guo Z, et al. Aqueous flexible all-solid-state NiCo-Zn batteries with high capacity based on advanced ion-buffering reservoirs of NiCo2O4. Adv Compos Hybrid Mater 2022;5. https://doi.org/10.1007/s42114-021-00375-1.

[60] Li Y, Yang W, Liu X, Che S, Tu Z, Hou L, et al. Dual interface engineering of NiO/NiCo2O4/CoO heterojunction within graphene networks for high-performance lithium storage. Electrochim Acta 2021;389:138536. https://doi.org/10.1016/j.electacta.2021.138536.

[61] Greskovich C. The kinetics of NiCr2O4 formation and diffusion of Cr3+ ions in NiO. 1940. p. 279–81.

[62] Zhang Z, Li J, Yi T, Sun L, Zhang Y, Hu X, et al. Surface density of synthetically tuned spinel oxides of Co3+ and Ni3+ with enhanced catalytic activity for methane oxidation. Cuihua Xuebao/Chinese J Catal 2018;39:1228–39. https://doi.org/10.1016/S1872-2067(18)63055-4.

[63] Cai L, Li Y, Xiao X, Wang Y. The electrochemical performances of NiCo2O4 nanoparticles synthesized by one-step solvothermal method. Ionics 2017;23:2457–63. https://doi.org/10.1007/s11581-017-2084-z.

[64] Liu S, An C, Chang X, Guo H, Zang L, Wang Y, et al. Optimized core–shell polypyrrole-coated NiCo2O4 nanowires as binder-free electrode for high-energy and durable aqueous asymmetric supercapacitor. J Mater Sci 2018;53:2658–68. https://doi.org/10.1007/s10853-017-1742-x.

[65] Jiang W-J, Gu L, Li L, Zhang Y, Zhang X, Zhang L-J, et al. Understanding the high activity of Fe–N–C electrocatalysts in oxygen reduction: Fe/Fe3C nanoparticles boost the activity of Fe–nx. J Am Chem Soc 2016;138:3570–8. https://doi.org/10.1021/jacs.6b00757.

[66] Guan C, Liu X, Ren W, Li X, Cheng C, Wang J. Rational design of metal-Organic Framework derived Hollow NiCo2O4 Arrays for flexible supercapacitor and electrocatalysis. Adv Energy Mater 2017;7:1–8. https://doi.org/10.1002/aenm.201602391.

[67] Tong X, Pang N, Qu Y, Yan C, Xiong D, Xu S, et al. 3D urchin-like NiCo2O4 coated with carbon nanospheres prepared on flexible graphite felt for efficient bifunctional electrocatalytic water splitting. J Mater Sci 2021;56:9961–73. https://doi.org/10.1007/s10853-021-05892-4.

[68] Xiao X, Zhang X, Zhang Z, You J, Liu S, Wang Y. Macro-/meso-porous NiCo2O4 synthesized by template-free solution combustion to enhance the performance of a nonenzymatic amperometric glucose sensor. Microchim Acta 2020;187. https://doi.org/10.1007/s00604-019-4063-8.

[69] Wang A, Hu Y, Wang H, Cheng Y, Thomas T, Ma R, et al. Activating inverse spinel NiCo2O4 embedded in N-doped carbon nanofibers via Fe substitution for bifunctional oxygen electrocatalysis. Mater Today Phys 2021;17. https://doi.org/10.1016/j.mtphys.2021.100353.

[70] Kaneko R, Chowdhury TH, Wu G, Kayesh ME, Kazaoui S, Sugawa K, et al. Cobalt-doped nickel oxide nanoparticles as efficient hole transport materials for low-temperature processed perovskite solar cells. Sol Energy 2019;181:243–50. https://doi.org/10.1016/j.solener.2019.01.097.

[71] Tippo P, Thongsuwan W, Wiranwetchayan O, Kumpika T, Kantarak E, Singjai P. Influence of Co concentration on properties of NiO film by sparking under uniform magnetic field. Sci Rep 2020;10:1–12. https://doi.org/10.1038/s41598-020-72883-x.

[72] Wang H, Wang H, Huang J, Zhou X, Wu Q, Luo Z, et al. Hierarchical mesoporous/Macroporous Co-doped NiO nanosheet Arrays as free-Standing electrode materials for rechargeable Li-O2 batteries. ACS Appl Mater Interfaces 2019;11:44556–65. https://doi.org/10.1021/acsami.9b13329.

[73] Béjar J, Álvarez-Contreras L, Ledesma-García J, Arjona N, Arriaga LG. Electrocatalytic evaluation of Co3O4 and NiCo2O4 rosettes-like hierarchical spinel as bifunctional materials for oxygen evolution (OER) and reduction (ORR) reactions in alkaline media. J Electroanal Chem 2019;847:113190. https://doi.org/10.1016/j.jelechem.2019.113190.

[74] Yang L, Zhang B, Fang B, Feng L. A comparative study of NiCo2O4 catalyst supported on Ni foam and from solution residuals fabricated by a hydrothermal approach for electrochemical oxygen evolution reaction. Chem Commun 2018;54:13151–4. https://doi.org/10.1039/c8cc08251k.

[75] Wang Y, Liu T, Fang S, Xiao G, Wang H, Chen F. A novel clean and effective syngas production system based on partial oxidation of methane assisted solid oxide co-electrolysis process. J Power Sources 2015;277:261–7. https://doi.org/10.1016/j.jpowsour.2014.11.092.

[76] Flores CLI, Balela MDL. Electrocatalytic oxygen evolution reaction of hierarchical micro/nanostructured mixed transition cobalt oxide in alkaline medium. J Solid State Electrochem 2020;24:891–904. https://doi.org/10.1007/s10008-020-04530-4.

[77] Zhou LN, Yu L, Liu C, Li YJ. Electrocatalytic activity sites for the oxygen evolution reaction on binary cobalt and nickel phosphides. RSC Adv 2020;10:39909–15. https://doi.org/10.1039/d0ra07284b.

[78] Zheng Y, Wang J, Yu B, Zhang W, Chen J, Qiao J, et al. A review of high temperature co-electrolysis of H2O and CO2 to produce sustainable fuels using solid oxide electrolysis cells (SOECs): advanced materials and technology. Chem Soc Rev 2017;46:1427–63. https://doi.org/10.1039/c6cs00403b.

[79] Liu Q, Bian B, Fan J, Yang J. Cobalt doped Ni based ordered mesoporous catalysts for CO2 methanation with enhanced catalytic performance. Int J Hydrogen Energy 2018;43:4893–901. https://doi.org/10.1016/j.ijhydene.2018.01.132.

[80] Varun Y, Sreedhar I, Singh SA. Highly stable M/NiO–MgO (M = Co, Cu and Fe) catalysts towards CO2 methanation. Int J Hydrogen Energy 2020;45:28716–31. https://doi.org/10.1016/j.ijhydene.2020.07.212.

[81] Cho DY, Song SJ, Kim UK, Kim KM, Lee HK, Hwang CS. Spectroscopic investigation of the hole states in Ni-deficient NiO films. J Mater Chem C 2013;1:4334–8. https://doi.org/10.1039/c3tc30687a.

[82] Zhang B, Zheng X, Voznyy O, Comin R, Bajdich M, García-Melchor M, et al. Homogeneously dispersed multimetal oxygen-evolving catalysts. Science 2016;352:333–7. https://doi.org/10.1126/science.aaf1525. 80-.

[83] Chang CF, Hu Z, Wu H, Burnus T, Hollmann N, Benomar M, et al. Spin blockade, orbital occupation, and charge ordering in La1.5Sr0.5CoO4. Phys Rev Lett 2009;102:5. https://doi.org/10.1103/PhysRevLett.102.116401. 0–.

[84] Gutiérrez A, Domínguez-Cañizares G, Krause S, Díaz-Fernández D, Soriano L. Thermal induced depletion of cationic vacancies in NiO thin films evidenced by x-ray absorption spectroscopy at the O 1s threshold. J Vac Sci Technol, A 2020;38:033209. https://doi.org/10.1116/6.0000080.

[85] Chang TC, Lu YT, Lee CH, Gupta JK, Hardwick LJ, Hu CC, et al. The effect of degrees of inversion on the electronic structure of spinel NiCo2O4: a density functional theory study. ACS Omega 2021;6:9692–9. https://doi.org/10.1021/acsomega.1c00295.

[86] Tian C, Nordlund D, Xin HL, Xu Y, Liu Y, Sokaras D, et al. Depth-dependent redox behavior of LiNi 0.6 Mn 0.2 Co 0.2 O 2. J Electrochem Soc 2018;165:A696–704. https://doi.org/10.1149/2.1021803jes.

[87] Chang HW, Dong CL, Lu YR, Huang YC, Chen CL, Chen JL, et al. Ex-situ soft X-ray absorption spectroscopic investigation of NiCo2O4 annealed in different gases for hydrogen generation by electrolysis of urea. Int J Hydrogen Energy 2019;44:15771–8. https://doi.org/10.1016/j.ijhydene.2018.10.108.

[88] Cui M, Ding X, Huang X, Shen Z, Lee T-L, Oropeza FE, et al. Ni3+-Induced hole states enhance the oxygen evolution reaction activity of NixCo3−xO4 electrocatalysts. Chem Mater 2019;31:7618–25. https://doi.org/10.1021/acs.chemmater.9b02453.

[89] Davydova ES, Manikandan M, Dekel DR, Sunde S. Effect of the synthetic method on the properties of Ni-based hydrogen oxidation catalysts. ACS Appl Energy Mater 2021;4:3404–23. https://doi.org/10.1021/acsaem.0c03157.

[90] Cai X, Sun W, Xu C, Cao L, Yang J. Highly selective catalytic reduction of NO via SO2/H2O-tolerant spinel catalysts at low temperature. Environ Sci Pollut Res 2016;23:18609–20. https://doi.org/10.1007/s11356-016-7061-y.

[91] Yi Y, Zhang P, Qin Z, Yu C, Li W, Qin Q, et al. Low temperature CO oxidation catalysed by flower-like Ni-Co-O: How physicochemical properties influence catalytic performance. RSC Adv 2018;8:7110–22. https://doi.org/10.1039/c7ra12635b.

[92] Błaszczak P, Mizera A, Bochentyn B, Wang SF, Jasiński P. Preparation of methanation catalysts for high temperature SOEC by β-cyclodextrin-assisted impregnation of nano-CeO2 with transition metal oxides. Int J Hydrogen Energy 2022;47:1901–16. https://doi.org/10.1016/j.ijhydene.2021.10.144.

[93] Niu J, Liu H, Zhang Y, Wang X, Han J, Yue Z, et al. NiCo2O4 spinel for efficient toluene oxidation: the effect of crystal plane and solvent. Chemosphere 2020;259:127427. https://doi.org/10.1016/j.chemosphere.2020.127427.

[94] Greluk M, Rotko M, Turczyniak-Surdacka S. Enhanced catalytic performance of La2O3 promoted Co/CeO2 and Ni/CeO2 catalysts for effective hydrogen production by ethanol steam reforming. Renew Energy 2020;155:378–95. https://doi.org/10.1016/j.renene.2020.03.117. https://doi.org.

[95] Yao Y, Goodman DW. Direct evidence of hydrogen spillover from Ni to Cu on Ni–Cu bimetallic catalysts. J Mol Catal Chem 2014;383–384:239–42. https://doi.org/10.1016/j.molcata.2013.12.013. https://doi.org.

[96] Duch M, Esteve J, Gomez E, Perez-Castillejos R, Valles E. Electrodeposited Co-Ni alloys for MEMS. J Micromech Microeng 2002;12:400–5. https://doi.org/10.1088/0960-1317/12/4/309.

[97] Karimzadeh A, Aliofkhazraei M, Walsh FC. A review of electrodeposited Ni-Co alloy and composite coatings: microstructure, properties and applications. Surf Coating Technol 2019;372:463–98. https://doi.org/10.1016/j.surfcoat.2019.04.079. https://doi.org.